# The pressure–temperature–time–deformation history of the Beni Mzala unit (Upper Sebtides, Rif belt, Morocco): Refining the Alpine tectono-metamorphic evolution of the Alboran Domain of the western Mediterranean

Sara Marrone, Patrick Monie, Federico Rossetti, Federico Lucci, Thomas Theye, Mohamed Bouybaouene, Mohamed Najib Zaghloul

# The Pressure-Temperature-time-deformation history of the Beni Mzala unit (Upper Sebtides, Rif belt, Morocco): Refining the Alpine tectono-metamorphic evolution of the Alboran Domain of the Western Mediterranean

**Running Title**: **Alpine *P-T-t* evolution of the Alboran Domain**

Sara Marrone [1], Patrick Monié [2], Federico Rossetti [1*], Federico Lucci [1], Thomas Theye [3], Mohamed L. Bouybaouene [4] & Mohamed Najib Zaghloul [5]

[1] *Dipartimento di Scienze, Università Roma Tre, 00146 Rome, Italy*

[2] *Géosciences Montpellier, Université de Montpellier, CNRS, Université des Antilles, Montpellier, France.*

[3] *Institut für Anorganische Chemie, Universität Stuttgart, Stuttgart, Germany.*

[4] *Département de Géologie, Université de Rabat, BP 1014 Rabat, Morocco*

[5] *Département de Sciences de la Terre et d'Océanologie de l'Université ''Abdel Maleek Essâdi'' de Tanger, Tangier, Morocco*

*Corresponding Author:
Dipartimento di Scienze, Università Roma Tre
Sezione Scienze Geologiche
Largo San Leonardo Murialdo, 1
00146 Roma (Italy)
e-mail: federico.rossetti@uniroma3.it
Tel.: +39 06 5488 8043

This article has been accepted for publication and undergone full peer review but has not been through the copyediting, typesetting, pagination and proofreading process, which may lead to differences between this version and the Version of Record. Please cite this article as doi: 10.1111/JMG.12587

## ABSTRACT

The structural and thermal relaxation overprint associated with the Neogene Alboran rifting have obscured the early Alpine tectono-metamorphic evolution of the Alboran Domain, representing the metamorphic core of the Betic-Rif orogen of the western Mediterranean region. This study focuses on the Beni Mzala unit, forming the lower and deeper structural level of the Alpine metamorphic nappe stack (Upper Sebtides) in the Moroccan Rif. Meso- and micro-scale structural investigations are carried out on high-pressure aluminum silicate (Ky-bearing)-quartz segregations that occur as boudins within the main retrogressive syn-greenschist foliation ($S_2$/$D_2$) and assumed to preserve the early $M_1$ H*P* metamorphism associated with the Alpine orogenic construction in the Alboran Domain. These boudins host an early crenulated high-pressure foliation ($S_1$/$D_1$) made of quartz-kyanite-white mica-rutile. A large spread in white mica composition is documented, with the highest Si content per formula unit (up to 3.18 apfu) preserved along the $S_1$ foliation and the lower Si content observed in the white micas marking the $S_2$ foliation and the rim of $S_1$ micas. Microtextural evidence documents post-tectonic andalusite growth and static recrystallisation of the quartz microlithons. Inverse (Zr-in-Rt thermometry) and forward modelling thermobarometry are integrated with Ar-Ar white mica geochronology to define the peak and exhumation pressure-temperature-time (*P*-*T*-*t*) path of the Beni Mzala unit. Minimum thermo-baric estimates for the $M_1$ event are ca. 1.4 GPa and 600 °C, corresponding to a metamorphic gradient of ca. 11°/km, consistent with subduction zone metamorphism. Exhumation is constrained by re-equilibration of the white mica composition (from high to low celadonite) between ca. 29 and 22 Ma, during a nearly isothermal retrogressive path, with final equilibration at high-temperature/low-pressure conditions within the andalusite stability field (ca. 0.2-0.3 GPa and 500 °C). A minimum late Oligocene age is proposed for the Alpine $D_1$ tectono-metamorphic stage in the Rif, suggesting as feasible the previously proposed Eocene timing for the subduction-zone metamorphism of the Alboran Domain. Conclusive evidence is provided to link the early Miocene tectono-metamorphic event to a late thermal perturbation that affected the Alboran Domain at shallow crustal conditions, post-dating the almost complete exhumation of the deep roots of the Alpine belt in the western Mediterranean.

**Keywords**: Alpine orogeny, tectono-metamorphic evolution, Ar-Ar geochronology, Alboran Domain, Mediterranean region

## 1. INTRODUCTION

Metamorphic rocks recovered from fossil subduction zones provide key information on the thermal structure, rheological conditions and geochemical processes that operated at depth within the subduction channel (e.g., Agard, Plunder, Angiboust, Bonnet, & Ruh, 2018; Bebout, 2014; Malusà et al., 2015; Maruyama, Liou, & Terabayashi, 1996; Monié & Agard, 2009; Peacock, 1996; Penniston-Dorland, Kohn, & Manning, 2015; Plunder, Agard, Chopin, Pourteau, & Okay, 2015). The pressure-temperature-time-deformation (*P-T-t-d*) history derived from exhumed metamorphic terranes along fossil and active convergence zone may thus contribute to constrain the evolving geodynamic scenarios and tectonic processes associated with orogenic construction and destruction at convergent plate boundaries.

As a part of the Mesozoic-Cenozoic Alpine-Himalayan convergent zone, the exhumed roots of the Alpine orogen exposed along the Mediterranean region (Figure 1a), has provided a natural laboratory to parameterize the tectonic regimes and characterize the geodynamic processes that control the space-time evolution of mountain belts in general. Although the first-order spatio-temporal picture of the geodynamic and paleotectonic evolution is now acquired (e.g. Faccenna et al., 2014; Handy, Schmid, Bousquet, Kissling, & Bernoulli, 2010; Jolivet, Faccenna, Goffé, Burov, & Agard, 2003; van Hinsbergen et al., 2020), major uncertainty still remains on the geodynamic reconstructions of the Western Mediterranean region as derived from the exhumed metamorphic roots of the Betic-Rif orogen (Spain-Morocco), the so-called Alboran Domain (e.g., Michard et al. 2006; Figure 1b). In fact, while several and contrasting tectonic and geodynamic models have been proposed in the literature by the study of the Alboran Domain units (e.g., Azañón & Crespo-Blanc, 2000; Booth-Rea, Azañón, Martínez-Martínez, Vidal, & García-Dueñas, 2005; Frasca et al., 2017; Garrido et al., 2011; Gueydan, Mazzotti, Tiberi, Cavin, & Villaseñor, 2019; Hidas et al., 2013; Hommonay et al., 2018; Mazzoli et al., 2013; Michard et al., 2002; Platt & Vissers, 1989; Platt, Anczkiewicz, Soto, Kelley, & Thirlwall, 2006; Platt, Whitehouse, Kelley, Carter, & Hollick, 2003a; Platt et al., 2003b; Tubía, Cuevas, & Esteban, 2004; Van der Wal & Vissers, 1993; Williams & Platt, 2018; Zeck, 1996), still poorly constrained are (i) the timing of Alpine orogenic construction and subduction zone metamorphism in the region and (ii) the evolving tectonic/geodynamic regimes driving the Alpine structuration of the Rif-Betic orogen. Both elements hampering a full assessment of the tectonic correlations at regional scale as well as the paleotectonic reconstructions.

Through a multidisciplinary research approach that integrates fieldwork with laboratory analysis, this study is aimed at providing new *P-T-t-d* constraints to the orogenic construction of the Western Mediterranean by focusing on the H*P*/L*T* remnants of the subduction zone metamorphism (Beni Mzala units of the Upper Sebtides) exposed in the Alboran Domain of the Rif belt of northern

Morocco (Figures 1a, 2a). We document a metamorphic evolution from high- to low-pressure conditions, spanning from the late Oligocene (ca. 29 Ma) to the early Miocene (ca. 22-21) Ma that we link to the transition from syn-orogenic exhumation of the subduction channel units to the post-orogenic crustal thinning of the Betic-Rif realm. We assume that the late Oligocene is a minimum age for the timing of Alpine orogeny in Western Mediterranean. These results provide essential information for constraining timing and rates of tectonic processes during orogenic construction at regional scale and for a better understanding of the Alpine geodynamics of the Mediterranean region more generally.

## 2. GEOLOGICAL BACKGROUND

The Alboran Domain forms the metamorphic core of the Betic-Rif orogen, an arcuate mountain belt developed at the front of the westward retreating Mediterranean subduction zone (Faccenna et al., 2004; Jolivet et al., 2008; Platt, Behr, Johanesen, & Williams, 2013). The Alboran Domain consists of continental-derived metamorphic units, with polyphase tectono-metamorphic evolution (Variscan and Alpine; Rossetti et al., 2020 and references therein) that can be correlated across the Betic-Rif chain (Michard et al., 2006). In the Rif belt of northern Morocco (Figure 2a), the Alboran Domain is made up of three main rock complexes that are overthrusted onto the Maghrebian Flysch, from bottom to top (Chalouan & Michard, 2004; Kornprobst, 1974; Michard et al., 2006): (i) the carbonate units of the Dorsale Calcaire; (ii) the Ghomaride (Malaguide in Spain) Complex (low-grade Paleozoic basement rocks unconformably covered by discontinuous Mesozoic-Tertiary deposits); and (iii) the Sebtide (Alpujarride in Spain) Complex, a nappe stack of metamorphic units with distinct low- and high-grade metamorphic signatures. The structurally lowermost tectonic unit is made up by the metapelites of the Nevado-Filabride Complex of the Betics (Li & Massonne, 2018; Martínez-Martínez, Soto, & Balanyá, 2002; Platt, Anczkiewicz, Soto, Kelley, & Thirlwall, 2006), not exposed in the Moroccan Rif.

The Alpujarride-Sebtide realm host large peridotite bodies (Ronda in the Betics and Beni Bousera in the Rif) enclosed in polymetamorphic (Variscan and Alpine) granulite facies crustal envelopes (Acosta-Vigil et al., 2014; Guedydan et al., 2015; Melchiorre et al., 2017; Montel, Kornprobst, & Vielzeuf, 2000; Rossetti et al., 2010, 2020; Sánchez-Navas, García-Casco, Mazzoli, & Martín-Algarra, 2017; Zeck & Williams, 2001; Zeck & Whitehouse, 2002)

Regarding the metamorphic signature, the Alpujarride-Sebtide units records a low grade, subduction-type metamorphism on Permian-Triassic protoliths and a high-grade Barrovian-type metamorphism on pre-Alpine protoliths (Azañón, García-Dueñas, & Goffé, 1998; Azañón & Crespo-Blanc, 2000; Bouybaouene, Goffé, & Michard, 1995; El Maz & Guiraud, 2001; Goffé, Azañón, Bouybaouene, & Jullien, 1996; Gueydan et al. 2015; Homonnay et al., 2018; Michard et al., 2006; Rodríguez-Ruiz, Abad, & Bentabol, 2019; Ruiz Cruz, De Galdeano, Álvarez-Valero, Rodriguez Ruiz, & Novák, 2010; Vidal, Goffé, Bousquet, & Parra, 1999), respectively, with a marked downward increase in the paleo-temperature gradients, commonly referred to the heat source provided by the intracrustal emplacement of the peridotite bodies (Negro, Beyssac, Goffé, Saddiqi, & Bouybaouene, 2006).

Most of the available radiometric geochronological (U-(Th)-Pb dating on zircons and monazites: Frasca et al., 2017; Gueydan et al., 2015; Homonnay et al., 2018; Janots et al., 2006; Massonne, 2014; Melchiorre et al., 2017; Platt & Whitehouse, 1999; Platt et al., 1998; Platt et al., 2003a; Rossetti et al., 2010, 2020; Sánchez-Rodríguez & Gebauer, 2000; Zeck & Whitehouse 1999, 2002; Zeck & Williams, 2001; K-Ar and Ar-Ar datings: Frasca et al., 2017; Homonnay et al., 2018; Loomis, 1975; Michard et al., 2006; Monié, Galindo-Zaldivar, Lodeiro, Goffé & Jabaloy, 1991; Monié, Torres-Roldán, & García-Casco, 1994; Pearson, Davies, & Nixon, 1993; Platt et al., 1998; Platt et al., 2003a,b; Zeck, Monié, Villa, & Hansen, 1992) and low-temperature thermochronological (fission-track and (U-Th)/He thermochronology on zircon and apatite: Andriessen & Zeck, 1996; Azdimousa et al., 2014; Platt et al., 1998; Romagny et al., 2014) data for the Alpine tectono-metamorphic evolution of the Alpujarride-Sebtide Complex cluster at 24-18 Ma (early Miocene) and are commonly interpreted in terms of cooling and exhumation of the Alboran domain. Nonetheless, different tectonic and geodynamic scenarios have been proposed in the literature to frame the early Miocene exhumation of the Alboran Domain, either including orogenic collapse and delamination of the orogenic roots (Platt & Vissers, 1989; Platt et al., 1998, 2003a; Williams & Platt, 2018), hot thrusting (Tubía & Cuevas, 1987), transpressional shearing (Mazzoli & Martín-Algarra, 2011; Mazzoli et al., 2013) or a switch from back-arc extension to thrusting (Azañon & Crespo Blanc, 2000; Booth Rea et al., 2005; Frasca et al., 2017; Gueydan et al., 2019; Hidas et al., 2013). Significantly, the early Miocene times also corresponds to (i) the onset of back-arc extension leading to the opening of the Neogene Alboran basin (e.g., Booth-Rea, Ranero, Martínez-Martínez, & Grevemeyer, 2007; Comas, Platt, Soto, & Watts, 1999; Dewey, 1988; Faccenna, Becker, Lucente, Jolivet, & Rossetti, 2001, Faccenna et al., 2004; García-Dueñas, Balanyá, & Martínez-Martínez, 1992; Guerrera, Martín-Martín, & Tramontana, 2019; Jolivet & Faccenna, 2000; Jolivet et al., 2008; Michard et al., 2006; Platt & Vissers, 1989; Platt & Whitehouse, 1999; Platt et al., 1998, 2003a,b; Platt et al., 2013; Rosenbaum, Lister, & Duboz, 2002; van Hinsbergen, Vissers, & Spakman, 2014; Vergés & Fernàndez, 2012) and (ii) to a major episode of regional magmatism (Esteban, Cuevas, Tubía, Sergeev, & Larionov 2010; Rossetti et al., 2010; Rossetti, Dini, Lucci, Bouybaouene, & Faccenna, 2013; Turner et al., 1999).

Still largely debated is the timing of the Alpine H*P*/L*T* subduction-zone metamorphism and crustal thickening in the Alboran Domain, also due to the pervasive early Miocene tectono-thermal overprint, which obscured the early tectono-metamorphic evolution (e.g. Monié, Galindo-Zaldivar, Lodeiro, Goffé & Jabaloy, 1991). However, a Paleogene age is commonly assumed in most of the tectonic reconstructions (e.g., Azañón et al., 1998; Azañón & Crespo-Blanc, 2000; Booth-Rea et al., 2005; Chalouan et al., 2008; Faccenna et al., 2004; Malusà et al., 2015; Michard et al., 2006; Platt & Vissers, 1989; Platt et al., 2013; Rossetti, Faccenna, & Crespo-Blanc, 2005; Vergés & Fernàndez, 2012; Williams & Platt, 2018; Zeck, 1997), albeit framed within different geodynamic scenarios for the Mesozoic-Cenozoic subduction of the Alpine Tethys in the Western Mediterranean (i.e., the two ("Eo-Alpine" and "Apennine- Maghrebian") subduction *vs* the single ("Apennine- Maghrebian") subduction models; e.g., Carminati, Lustrino, & Doglioni, 2012; Doglioni, Gueguen, Harabaglia, & Mongelli, 1999; Faccenna et al., 2004; Handy et al., 2010; Herwegh et al., 2020; Jolivet & Faccenna, 2000; Michard, Chalouan, Feinberg, Goffé, & Montigny, 2002; Michard et al. 2006; Molli & Malavieille, 2011; Rosenbaum et al., 2002; van Hinsbergen et al., 2020). The few available geochronological data derived from the Betics, based on white mica Ar-Ar geochronology (Alpujarrides: Platt, Kelley, Carter, & Orozco, 2005; Nevado Filabrides: Augier et al., 2005; Monié, Galindo-Zaldivar, Lodeiro, Goffé & Jabaloy, 1991) and electron microprobe dating of monazite (Alpujarride Complex: Massonne, 2014; Nevado Filabride Complex: Li & Massonne, 2018), suggest an Eocene age (ca. 50-34 Ma) for the H*P* metamorphism in the Alboran Domain. Nonetheless, based on Lu-Hf garnet dating, an early Miocene timing (18-14 Ma) has been also proposed for the subduction zone metamorphism in the Nevado Filabride Complex (Platt, Anczkiewicz, Soto, Kelley, & Thirlwall, 2006).

For the Rif, a minimum age of ca. 28 Ma was proposed for the Alpine orogeny, based on white mica Ar-Ar geochronology (Michard et al., 2006) from the Upper Sebtides and U-Th-Pb monazite dating for the Lower Sebtides (Homonnay et al., 2018), respectively. An Eocene timing for the orogenic tectono-metamorphic evolution of the Alboran Domain is compatible with the stratigraphic evidence, documenting Oligocene-Aquitanian deposits unconformably covering the Ghomaride-Malaguide nappe stack (Chalouan et al., 2008; Durand-Delga, Feinberg, Magné, Olivier, & Anglada, 1993; Lonergan, 1993; Lonergan & Mange-Rajetzky, 1994; Serrano et al., 2006; Vergés & Fernàndez, 2012). The Eocene-Oligocene (ca. 44-28 Ma) detrital apatite and zircon fission track ages from the Oligocene-Miocene synorogenic deposits cropping out in the internal Betics further document erosional unroofing of the Alboran Domain during Eocene-Oligocene times (Lonergan & Johnson, 1998). Finally, a pre-Miocene timing for the Alpine orogenic construction in the Betic-Rif region is also supported by occurrence of metamorphic clasts sourced from the Alpujarride Complex in the early Miocene deposits of the external and internal zones of the Betics (e.g., Lonergan & Mange-Rajetzky, 1994; Serrano et al, 2006).

### 2.1 Regional Geology and previous studies

The Sebtide Complex in the Rif belt crops out within four antiformal structures, Beni Mzala, Ceuta, Cabo Negro and Beni Bousera, from north to south (Kornprobst, 1974; Michard et al., 2006) (Figure 2a). The Sebtides are divided into the Upper Sebtides (Federico units) and the Lower Sebtides (Filali units), which, traditionally described with subduction- and Barrovian-type metamorphic signature, respectively (Bouybaouene et al., 1995; Bouybaouene, Michard, & Goffé, 1998; El Maz & Guiraud, 2001; Gueydan et al., 2015; Michard, Goffé, Bouybaouene, & Saddiqi, 1997; Michard et al., 2006; Negro et al., 2006; Rodríguez-Ruiz et al., 2019; Ruiz Cruz et al., 2010), form the envelope of the Beni Bousera units (migmatitic granulites and the Beni Bousera peridotites; Álvarez-Valero et al., 2014; Bouybaouene et al., 1998; Kornprobst, 1974; Melchiorre et al., 2017; Rossetti et al., 2020).

The Federico units consist of four tectonic slices with the same stratigraphic succession, which underwent different peak *P-T* conditions ($M_1$ stage) in the paleo-subduction channel, from the shallowest to the deepest: the Tizgarine (TZ), Boquete Anjera (BA), Beni Mzala-2 (BM2) and Beni Mzala-1 (BM1) units. Their lithostratigraphic structure includes Upper Paleozoic greywakes, Permo-Triassic reddish to greyish phyllites, Triassic quartzites and dolostones (Bouybaouene et al., 1995; Chalouan & Michard, 2004; Michard et al., 2006; Zaghloul, 1994). Each tectonic unit is characterized by its own thermo-baric evolution, typified by nearly isothermal or cooling exhumation path, with final equilibration under low greenschist facies conditions ($M_2$ retrogressive stage) (Bouybaouene et al., 1995; Rodríguez-Ruiz et al., 2019; Ruiz Cruz et al., 2010; Vidal et al., 1999) (Figure 2b). In TZ, the $M_1$ assemblage cookeite-pyrophyllite-phengite (low-substituted) corresponds to L*P*–L*T* (0.3-0.4 GPa and 300 °C) metamorphic conditions. In BA, the $M_1$ assemblage sudoite-Mg-chlorite-phengite-(Fe-Mg)-chloritoid indicates ca. 0.7 GPa and 300–380 °C. In BM2, occurrence of Mg-carpholite as relics in chloritoid-quartz or kyanite-quartz veins indicates $M_1$ blueschist-facies conditions of 0.8-1.3 GPa and 380-450°C. Finally, in BM1, Mg-carpholite relics in Mg-chloritoid-quartz veins, and talc-phengite assemblages in quartz-kyanite segregations testify to $M_1$ eclogite-facies conditions, between 1.3–1.5 GPa, 450°C, and 1.5–1.8 GPa, 550°C (Vidal et al. 1999).

Structures in both Federico units and the underlying Filali micaschists are characterized by a pervasive plano-linear (S-L) tectonic fabric, with a dominant top-to-the-NNW (present coordinates) sense of shear (Gueydan et al., 2015; Michard et al., 2006; Negro et al., 2006). The available geochronological data from the Federico units as derived from K-Ar and $^{40}Ar/^{39}Ar$ mica (clay-mica mixtures, muscovite and biotite) geochronology span from late Oligocene (ca. 28-25 Ma) to the early Miocene (ca. 24-20 Ma) (Michard et al., 2006). However, a systematic study of the age-composition relationships of the different mica population is still missing. Early Miocene ages are also derived from U-(Th)-Pb dating of light REE accessory minerals (allanite-rich epidotes and phosphates) from the Federico units and referred to the retrograde, syn-exhumation tectono-metamorphic evolution (Janots et al., 2006).

## 3. MATERIALS AND METHODS

The research rationale is conceived to reconstruct the *P-T-t-d* evolution of the H*P* BM1 unit that, recording the peak of subduction zone metamorphism in the Alboran Domain, is used as proxy to refine the timing, *P-T* and deformation regimes of the Alpine orogeny in the Western Mediterranean region. A multidisciplinary approach is adopted that combines field work and structural (meso-and micro-scale) investigations with laboratory (petrological and Ar-Ar geochronological) work. Structural investigations were carried out within the Beni Mzala and Beni Bousera antiforms (Figure 2a, c-d) in order to define the tectono-metamorphic setting of the BM1 unit and to sample representative lithologies for laboratory work. Due to the intense and pervasive metamorphic retrogression that characterizes the BM1 unit at the outcrop scale, sampling focused on cm to dm-scale boudins of syn-metamorphic aluminum silicate-bearing quartz segregations (Qz-Ky, hereafter referred as $V_1$ veins) that are assumed to better preserve the peak H*P* parageneses (see below). Location of the collected samples, together with their constituent mineralogy and the adopted analytical methods are shown in Table S1. Electron microprobe analyses (EMPA) were used to define compositions of the constituent mineral assemblages. Inverse and forward modelling thermobarometry (Powell & Holland, 2008) is used to assess the thermo-baric conditions associated with metamorphic peak and exhumation of the BM1 unit. *In situ* and step-heating $^{40}Ar/^{39}Ar$ white mica geochronology is used to constrain the timing of orogenic metamorphism and to derive the exhumation *P-T-t* path of the BM1 unit. Details on the analytical methods and protocols adopted in this study are provided in Appendix S1. Mineral abreviations are after Whitney & Evans (2010), complemented with Wm for white mica. In the following, if specified otherwise, the term Wm includes muscovite/phengite as well as paragonite/margarite.

## 4. FIELD DATA AND SAMPLE DESCRIPTION

In the Beni Mzala antiform, the BM units forms the core of a major, NNE-SSW trending antiformal structure, where the Alpine Federico units are exposed below the Ghomaride Complex (Figure 2a,c). The peak metamorphic conditions grade from the lower-greenschist facies in the Tizgarine unit to the blueschist- and eclogite-facies in the BM units (Bouybaouene et al., 1995; Ruiz Cruz et al., 2010; Vidal et al., 1999). Brittle tectonic contacts mark transitions among the different units, which correspond to major metamorphic gaps (Bouybaouene et al., 1995; Michard et al., 2006; Vidal et al., 1999). The tectono-metamorphic architecture of the Federico units is typified by a progressive transition from a low-grade $D_1/M_1$ to a composite, retrogressive $D_1/M_2$ plano-linear fabrics when moving down-section from the Tizgarine to the BM units. In the BM units, the H*P* $D_1/M_1$ tectono-metamorphic fabric is attested by a relic, crenulated $S_1$ foliation made of Qz-Wm-Chl-Mg-Car/Mg-Ctd associations and by boudins of cm-to-dm scale aluminum silicate-bearing quartz (Qz-Ky-Wm ± Mg-Car ± Mg-Ctd) vein segregations ($V_1$ veins) (see also Bouybaouene et al. 1995; Ruiz Cruz et al., 2010; Vidal et al., 1999). The $D_2/M_2$ fabric often transposes earlier structures and consists of S-L tectonites developed under greenschist facies metamorphic conditions. The $M_2$ mineral assemblage is made of Qz-Chl-Wm (secondary)-Pl ± Ca-Amp and typically defines a NNW-SSE trending $L_2$ stretching direction (Figure 3). $D_2$ finite deformation is partitioned between domains of coaxial stretching and domains of non-coaxial top-to-the-NNW shearing. Shear sense indicators are dominantly provided by S-C tectonites and asymmetric boudinage of early segregated $V_1$ veins (Figure 3a-b). An array of roughly E-W striking Qz-Chl veins ($V_2$), striking sub-perpendicular to the $L_2$ lineations, is associated with the development of the $S_2$-$L_2$ retrogressive fabric (Figure 2c).

In the Beni Bousera antiform, a continuous exposure of the Alboran Domain units crops out along the Oued Kannar section. The Federico units define a verticalised panel of tectonic units, interleaved between the Dorsale units to the west and the Filali unit to the east (Figure 2a, c). Similarly to the northern sector, a transition from $D_1$ to $D_2$ plano-linear fabrics is documented when moving from the Tizgarine to the BM units. The BM1 unit is exposed in ca. 2 km$^2$ outcrop at Souk el Had (Figure 2a; see also Michard et al., 2006), where a syn-greenshist $D_2/M_2$ plano-linear fabric defines the main foliation, enveloping cm-to dm scale boudins of early segregated aluminum silicate-quartz (Ky-Qz-Wm) segregations ($V_1$) (Figure 3d). The $D_2/M_2$ syn-greenschist assemblage again includes secondary Chl-Wm-Pl-Ep ± Ca-Amp assemblages, forming NNW-SSE trending $L_2$ stretching lineation (Figure 2a,d). The $D_2$ shear senses are less evident, but, when detectable, again point to top-to-the-NNW shearing. Significantly, the $L_2$ stretching directions are subparallel to the ones associated with the main plano-linear fabrics observed in the underlying Filali unit, where similar top-to-the-NNW shear senses are reported (Gueydan et al., 2015).

The studied samples (B3, 32 and 34; Figure 2a and Table S1) include $V_1$ segregations and the metamorphic selvages. The mineral assemblages are similar in all the studied samples, but rock textures vary with respect to the intensity of the $D_2/M_2$ retrogressive stage (Figures 4, 5). At the thin section scale, the $V_1$ mineral assemblage, best preserved in samples 32 and 34, consists of $M_1$ Qz-Ky-Wm1 ± Rt ± Hem, which typically occurs as microlithons within the $S_2$ syn-greenschist crenulation domains (Figures 4, 5). The modal abundance of Ky in $V_1$ ranges 15-20 vol.%. Typically, the Ky crystals (up to 1 cm in length) do not present any preferred orientation (Figure 6a-c) and they show evidence of bending, undulose extinction and/or fracturing (Figure 6d). Interfingering with Wm (Wm1, 5-10 vol.%) is usually observed, suggesting equilibrium growth textures with Ky (Figure 6c). Significantly, the Ky and Wm1 associations are crenulated along the $S_2$ foliation (Figure 6a). The modal abundance of Rt and Hem ranges 0.5-1 vol.% and are often hosted as inclusions in Ky (Figure 6e). The enveloping schistose matrix is dominated by the $M_2$ assemblage made of Chl-Wm2 (Figure 5), in association with post-kinematic Pl (anorthite rich), Ep ± Ca-Amp ± Pmp (Figure 6f). The late growth of Wm3 is also observed to fill cracks in Ky and to replace early segregated Wm1-2 crystals (Figure 5d,g,h). Significant is the presence of post-kinematic And overgrowing the $S_2$ foliation and late Cb veins in samples 32 and 34 (Figure 5i).

Microfabric of the Qz-veins is dominated by ductile deformation textures, as attested by prominent undulose extinction, subgrain formation and recrystallisation textures (Figure 7). The interlobated grain boundaries attest that grain boundary migration is the dominant recrystallisation process (Figure 7b, d), but evidence of subgrain rotation recrystallisation is also locally documented (Figure 7a), suggesting heterogeneous strain. Polygonization of the recrystallized quartz grains (Figure 7c, d) attests for post-deformation recovery (Passchier & Trouw, 2010).

## 5. WHITE MICA CHEMISTRY

In the following, the mineral chemistry as obtained from electron microprobe analyses (EMPA) of the different Wm generations in the $V_1$ veins and the metamorphic selvages is presented. Representative mineral compositions and formulae (see Appendix S1) from the complete dataset ($n$ = 177) are presented in Table 1, whereas the complete dataset is presented in Table S2.

The Wm1 ($n$ = 34) shows cores characterized by $SiO_2$ ranging 46.53-48.44 wt.%, with $Al_2O_3$ 32.83-36.37 wt.%, $FeO_{tot}$ 0.63-3.02 wt.%, MgO 0.58-1.26 wt.%, $Na_2O$ 0.32-1.40 wt.%, BaO up to 0.39 wt.%, CaO < 0.12 wt.% and Ca/K atomic ratio <0.01 (Table 1). The Cl content is always below the detection limit. The Si-content ranges 3.11-3.18 atoms per formula unit (apfu), with $Al_{tot}$

2.59-2.78 apfu, ($Fe^{2+}$+Mg) = 0.09-0.20 apfu and $Fe^{3+}$ up to 0.15 apfu and corresponding to $X_{Ms}$ = 0.59-0.71, $X_{Cel}$ = 0.11-0.19, $X_{Prl}$ = 0.02-0.13, $X_{Par}$ = 0.05-0.18 (Figure 8a,b).

The Wm2 (Wm1 rim compositions, main foliation and selvages; *n* = 122) micas are characterized $SiO_2$ in the range 45.27-47.93 wt.% with $Al_2O_3$ 33.23-36.34 wt.%, $FeO_{tot}$ 1.63-3.14 wt.% and MgO 0.28-1.22 wt.%. The Wm2 is distinctly higher in CaO (up to 1.61 wt.%), whereas the $Na_2O$ (0.44-1.49 wt.%) and BaO (up to 0.40 wt.%) are comparable to Wm1. The Wm2 shows Ca/K ratio up to 0.07 and Cl content always below the detection limit. The Wm2 population shows a large spread in Si, varying 3.02-3.14 apfu, with $Al_{tot}$ 2.63-2.85 apfu, ($Fe^{2+}$+Mg) = 0.04-0.20 apfu, and $Fe^{3+}$ up to 0.17 apfu and corresponding to values of $X_{Ms}$ = 0.57-0.83, $X_{Cel}$ = 0.02-0.14, $X_{Prl}$ = 0.00-0.16, $X_{Par}$ = 0.09-0.19 (Figure 8a,b).

Collectively, the studied Wm1 and Wm2 populations show a progressive evolution from high-Si (maximum value 3.18 apfu) Wm1 cores with high $X_{Cel}$ (maximum value 0.19) and low $Al_{tot}$+$Fe^{3+}$ (2.67-2.78 apfu, mean value 2.74 apfu) content, to low-Si (minimum value 3.02 apfu) Wm2, with low $X_{Cel}$ (minimum value 0.03) and high $Al_{tot}$+$Fe^{3+}$ (2.68-2.93 apfu, mean value 2.81 apfu) content. The Ca content might reflect an intergrowth of Wm1/Wm2 with tiny lamellae of margarite.

The texturally late Wm3 (*n* = 21) found both as filling product of cracks pulling apart the Ky crystals and as alteration lamellae overprinting Wm1-Wm2 aggregates is Ca-Al-rich (CaO: 4.65-10.18 wt.%; $Al_2O_3$: 42.52-54.81 wt.%), with variable $Na_2O$ (0.72-3.60 wt.%) and $K_2O$ (0.20-1.89 wt.%), corresponding essentially to margarite/paragonite solid solution. Variable K contents results from tiny inclusions of Wm1/Wm2. The Ca/K ratio ranges 2.44-41.74 and the Cl content is systematically below the detection limit (Table 1).

## 6. THERMOBAROMETRY

The thermo-baric environment of the $M_1$-$M_2$ metamorphism in the BM1 unit was assessed by focusing on the $V_1$ (Qz-Ky + Ms + Rt) vein segregations, considered to best preserve the early H*P* orogenic stage. We combine the pressure-dependent Zr-in-rutile thermometry of Tomkins, Powell, & Ellis (2007), with pseudosection modelling using the software program Perple_X version 6.8.9 (Connolly, 2005; http://www.perplex.ethz.ch/).

### 6.1 Zr-in-rutile thermometry

The composition of rutile crystals from the Ky-Qz domains in $V_1$ was investigated through EMPA (Table S3). The rutile composition shows FeO ranging 1.345-2.425 wt.%, $Nb_2O_5$ in the range 0.209-0.871 wt.% and $SiO_2$ <0.65 wt.%. Rutile grains show Zr in the range 53-326 ppm (average 155, $n$ = 20), corresponding to temperatures ranging (i) 511-633 ± 40°C (analytical uncertainty) at 0.5 GPa, (ii) 532-658 ± 40°C at 1.0 GPa, and (iii) 554-682 ± 40°C at 1.5 GPa, respectively. The corresponding lower (first quartile) and upper (third quartile) limits of the interquartile range (IRQ) values (Tomkins et al., 2007; Taylor-Jones & Powell, 2015) are 519-615 °C, 540-639 °C and 562-663 °C with a median value of 568 ± 45°C, 590 ± 46°C and 613 ± 47°C, respectively (Appendix S2).

**6.2 Pseudosection modelling**

To reconstruct the representative bulk $V_1$ whole-rock composition, we have integrated mineral modal percentages in sample 32 with the corresponding average compositions as derived from the EMPA (Appendix S3 and Table 1). *P-T* pseudosections were calculated in the $K_2O$–FeO–MgO–$Al_2O_3$–$SiO_2$–$H_2O$–$TiO_2$–$O_2$ (KFMASHTO), neglecting minor $Na_2O$ and CaO. The original ferric iron content of the rock is unknown. Therefore, the FeO/$Fe_2O_3$ for the pseudosection modelling is estimated by trial-and-error calculations to obtain the analysed ($Fe^{2+}$ + Mg) contents in phengite at the low P boundary of the low variance $V_1$ assemblage Qz-Ky-Wm-Rt-Hem. This is the case with about 50% of total iron being $Fe^{3+}$. Calculated $Fe^{3+}$ contents in Wm are in the same range but strongly scattering because (i) EMPA results are not precise enough for this purpose, and (ii) of simplified assumptions on stoichiometric constraints. The selected strategy affects the calculated assemblages but it has only a minor impact on the *P-T* positions of Si isopleths for Wm.

The following solid-solution models were used (details in the file solution.dat enclosed in the Perple_X package; database: hp04ver.dat, an updated version of the Holland & Powell (1998) thermodynamic dataset; Perple_X_6.8.9 version, downloaded March 26 2020): Pheng(HP) for white mica, Bio(HP) for biotite, Chl(HP) for chlorite, Ctd(HP) for chloritoid, and Gt(HP) for garnet. Additional end-member phases considered in the calculations comprise quartz, rutile, ilmenite, kyanite, sillimanite, hematite and magnetite. The pseudosections were constructed between 0.2 and 2.0 GPa and from 300° to 700 °C, assuming $H_2O$ in excess.

The results show that the peak $M_1$ assemblage made of Qz-Ky-Wm-Rt + Fe-Ox (Hem) in $V_1$ veins occurs at minimum $P$ of ca. 1.0 GPa at minimum $T$ of 550 °C (Figure 9). Combining the results from the Zr-in Rt thermometry with the Si isopleths as derived from the chemical compositions of the different generation of Wm (Wm1 and Wm2) it is possible to refine this estimate and to constrain the exhumation path of the BM1 unit. Considering the highest celadonite Wm1 composition in textural equilibrium with Ky (maximum Si = 3.18 apfu values; Table 1), the $M_1$ metamorphic climax in BM1 is constrained at ca. 1.4 GPa and 600 °C. The retrograde path from the $M_1$ to $M_2$ stage is constrained by (i) the absence of both Cld (low-T side) and Bt (high-T side) in the $M_2$ assemblage; and (ii) the Si isopleths for the low-substituted Wm2 compositions (3.02 < Si (apfu) < 3.14; Table 1), which impose a nearly isothermal decompression with a final equilibration within the And stability field (ca. 0.2-0.3 GPa and 500 °C) (Figure 9).

## 7. WHITE MICA $^{40}$AR/$^{39}$AR GEOCHRONOLOGY

The three samples (B3, 32 and 34) were investigated for *in situ* and step-heating laser probe laser $^{40}Ar/^{39}Ar$ dating. The adopted geochronological strategy was conceived with the aim to provide geochronological constrain of the main Wm growth stages ($M_1$ to $M_2$). *In situ* laser spot fusion experiments were performed on areas (usually 50-100 μm wide and 100-250 μm in length) where (i) equilibrium textures between Ky and Wm1 are best preserved and (ii) on the metamorphic selvages. Step-heating experiments were instead performed on single Wm grains (~500-700 µm each), separated from the rock matrix ($S_2$ foliation) (Figure 4). The analytical results are listed in Table 2 and 3 for *in situ* and step heating analyses, respectively.

A total of thirty-five UV laser $^{40}Ar/^{39}Ar$ *in situ* analyses were obtained from the three samples. Twenty-one spots were obtained from the Qz-Ky-Wm1 assemblages in the vein and fourteen from the selvages surrounding the veins (Figure 10). Data for the selected areas are reported in Figure 10 (a,b,f,j) to show the intra-sample distribution of $^{40}Ar/^{39}Ar$ ages in the analysed samples and the cumulative results are shown in Table 2. The *in situ* dating yielded age estimates spanning from early Miocene to late Oligocene, ranging 24.3±1.9-22.1±0.6 Ma for sample B3, 25.1±2.1-21.2±0.6 Ma for sample 32, and 28.6±2.0-22.3±1.2 Ma (±2σ analytical errors) for sample 34 (Figure 10 c,d,g,h,k,l; Table 2), respectively. Note that several mica analyses from the Ky-Qz boudins have high Ca/K ratios probably due to the degassing of margarite rich Wm3 that developed upon Wm1-Wm2 aggregates. Independently from the samples, the step-heating age spectra show nearly identical concordant plateau ages (Figure 10 e,i,m), pointing to early Miocene ages (21.7±0.1 Ma for sample B3, 21.9±0.1 Ma for sample 32 and 21.9±0.1 Ma for sample 34) for 50% and more of the $^{39}Ar$ released (Table 3).

## 8. DISCUSSION

The structural and petrographical evidence as reconstructed from the aluminum silicate-quartz $V_1$ veins in BM1 unit indicates that the Upper Sebtides experienced a polyphase metamorphic evolution typified by (i) a $M_1$ metamorphic peak equilibrated at H*P*/L*T* metamorphic conditions (ca. 1.4 GPa at 600 °C), and (ii) a metamorphic retrogression $M_2$ during a cooling exhumation path as constrained by the continuous chemical requilibration of the Wm1-Wm2 populations, with a final re-equilibration within the andalusite stability field (0.2-0.3 GPa and 450-

500°C). The final stages of the $M_2$ retrogression is associated with a significant Ca-metasomatism, as indicated by the post-kinematic growth of Ca-bearing assemblages (Pl, Ep, Ca-Amp ± Pmp), dominated by the texturally late growth of margarite rich Wm3 generation. This evidence agrees with the findings of Ruiz Cruz et al. (2010) from the aluminum silicate-quartz veins from the BM1 unit in the Beni Mzala antiform.

The quartz microfabric in $V_1$ segregations, documenting high-*T* (500-700 °C; Law, 2014; Passchier & Trouw, 2010; Stipp, Stünitz, Heilbronner, & Schmid, 2002) grain boundary migration recrystallisation as the dominant recrystallisation mechanism, is fully compatible with the thermal environment as derived from the Zr-in-Rt thermometry. Moreover, the evidence of post-deformation recovery of the recrystallized grains further confirms the static recrystallisation event attested by the post-tectonic growth of andalusite.

The $^{40}Ar/^{39}Ar$ geochronology provides a late Oligocene-early Miocene time span that can be interpreted in the light of this polyphase tectono-metamorphic evolution. The relative age probability plot derived from the cumulative *in situ* analyses shows a polymodal gaussian distribution, with the youngest age peak (22.39±0.25 Ma, ±2σ; corresponding to the 76% of the total data) given by micas from the main foliation. The spots from the boudinated H*P* $V_1$ segregations instead provide ages spanning between two endmembers at 27.71±0.32 Ma and 22.86±0.18 Ma (±2σ; corresponding to the 25% and 75% of the total data, respectively) (Figure 11a).

To better assess the significance of these age range, the different Ar reservoirs can be constrained by comparing the Ca/K and Cl/K values as calculated from the Ar isotope systematics ($^{37}Ar/^{39}Ar$ and $^{38}Ar/^{39}Ar$ values, respectively; Tables 2,3) with those obtained from the EMPA of the different Ms populations (e.g, Villa, 2010; Allaz, Engi, Berger, & Villa, 2011). Significantly, the EMPA indicate that Wm1 and Wm2 generations correspond to muscovite-phengite solid solution with minor pyrophyllite component, with Ca/K values ranging 0.0-0.07 and Cl/K ~0 (Cl is always below detection limit). The Ca-rich Wm3 and nearly pure margarite are texturally late, with Ca/K ranging 2.44-41.74±0.28 and Cl/K ~0 (Cl below detection limit). The $^{38}Ar/^{39}Ar$ values measured for the three dated samples are very low and confirm the quasi absence of Cl in the different micas.

The Ca/K *vs* age diagram (Figure 11b) for the *in situ* dating documents that the vast majority of the degassing patterns are compatible with Ca-poor Wm, with the oldest late Oligocene (at 28.0±0.3 Ma and 28.6±2.0 Ma) *in situ* ages obtained in the $V_1$ boudins. Wm1 phengite probably contributes to these ages that have to be considered as a minimum age for their crystallization due to the presence of Wm2 zoning that cannot be resolved by the laser. Younger ages obtained from the $V_1$ boudins and selvages correspond to different Ar reservoirs, since minor Ca contamination can be detected in relation with the degassing of margarite-rich Wm3 post-kinematic overgrowth (Figure 11b). The analysis with the highest Ca/K value provides an age of 22.4±1.3 Ma, in agreement with the plateau ages derived from the step-heating experiments, which provide, irrespective of the sample, early Miocene ages at ca. 22 Ma (Figure 10 e,i,m).

*In situ* ages up to 29 Ma once more question the meaning of $^{40}Ar/^{39}Ar$ ages in high-pressure rocks. In the present case, the rocks experienced peak temperature well above the commonly accepted closure temperature for argon in white micas, i.e. 450°C (Harrison, Célérier, Aikman, Hermann, & Heizler, 2009). However, many studies (e.g. Agard, Monié, Jolivet, & Goffé, 2002; Cao, Neubauer, Bernroider, & Genser, 2018; Di Vincenzo, Carosi, & Palmeri, 2004; Di Vincenzo, Tonarini, Lombardo, Castelli, & Ottolini, 2006; Laurent et al., 2017) suggest that the argon behaviour in high-pressure is strongly dependent of other factors than temperature, revealing that in addition to possible volume diffusion effects, the age variations in polydeformed high-pressure rocks are mostly under the control of recrystallisation and dissolution/precipitation effects (see Villa, 2010, 2016 for a discussion). In these studies, it is assumed that phengite can resist temperatures up to 550 °C without significant argon loss. Therefore, provided that excess argon is a negligible component, the age variations between 28 and 22 Ma can be interpreted to record the sequence of Wm (re)crystallizations from the metamorphic peak. Given the *P-T* path showing nearly isothermal decompression since the peak temperature at 600 °C (Figure 9) and the presence of post-kinematic andalusite, it is very likely that these ages record the low-pressure fast cooling of the Upper Sebtides in agreement with previous geochronological studies (see Homonnay et al., 2018; Rossetti et al., 2020 and references therein).

Based on the textural and compositional evidence, the $^{40}Ar/^{39}Ar$ Wm geochronology presented in this study thus constrains the post-thickening tectono-metamorphic evolution of the BM1 of the Alboran Domain in the Rif, during transition from high- to low-pressure conditions in a continuum exhumation path from the Ky to the And stability field. We can consequently propose a minimum late Oligocene age for the $D_1/M_1$ event. The syn-to-post $D_2/M_2$ top-to-the-NNW syn-greenschist shearing is instead placed during the Oligocene-Miocene transition, with the final metamorphic evolution firmly constrained at ca. 22 Ma. These results provide conclusive evidence that the Early Miocene corresponds to a period of crustal unloading and exhumation rather than burial and peak of metamorphism.

## 8.1 Implications at regional scale

The *P-T-t*-deformation history as derived from the H*P* BM1 unit bears important implications, dealing with (i) the timing, metamorphic gradients and tectonic regimes associated with the Alpine tectono-metamorphic evolution of the Alboran Domain of the Western Mediterranean, and (ii) the geodynamic scenario during orogenic construction at regional scale.

The *P-T* estimates for the $M_1$ metamorphic peak conform to a paleo-geothermal gradient of ca. 11°C/km (assuming a rock density of 2600 kg/m$^3$) and burial depth of ca. 55 km, in line with the thermal structure of the subduction channel as derived from the global record of fossil subduction zones (Agard et al., 2018; Penniston-Dorland et al., 2015). When compared with the available literature data, the climax of $M_1$ metamorphism as derived in this study is fully compatible with the subduction-zone metamorphism documented from the Permo-Triassic Alpujarride-Sebtides units (Azañón et al., 1998; Bouybaouene et al., 1995; Vidal et al., 1999). The Oligocene Wm ages derived from the H*P* Qz-Ky segregations are compatible with and confirm both the oldest Wm Ar-Ar dating results presented in Michard et al. (2006) for the Upper Sebtides and the U-Th-Pb monazite ages from the Lower Sebtides (Homonnay et al., 2018). However, due to the pervasive retrogression textures and chemical re-equilibration of the Wm population (Wm1 to Wm2) observed in the BM units, we do not exclude the possibility for an older timing for the Alpine subduction zone metamorphism in the Western Mediterranean (see also Homonnay et al., 2018; Michard et al., 2006; Monié, Torres-Roldán, & García-Casco, 1994). Therefore, the Eocene timing for the subduction zone tectono-metamorphic evolution of the Alboran Domain as proposed for Betics (Augier et al., 2005; Li & Massonne, 2018; Platt et al., 2005) seems a feasible scenario, being also compatible with the tectono-stratigraphic evidence as documented in Ghomaride-Malaguide nappe stack (Chalouan et al., 2008; Lonergan, 1993; Serrano et al., 2006).

The occurrence of post-tectonic And growth in BM1 indicates that the final stage of H*P* rock exhumation at shallow crustal conditions occurred under a rather hot paleo-geothermal environment (>40°C/km), at the waning stage of the $D_2$/$M_2$ event during the early Miocene. This evidence attests for the transition from subduction zone to Barrovian metamorphic gradients in the late stage of rock exhumation. Significantly, the post-tectonic growth of And is documented also in the higher grade units of the Alpujarride Complex of the Betics (Azañón et al., 1998; Rossetti et al., 2005; Simancas & Campos, 1993), suggesting a common Alpine tectono-metamorphic evolution for the entire Alpujarride-Sebtide realm. The early Miocene also corresponds to a major episode of crustal melting and granite magmatism across the entire Betic Rif realm (Esteban et al., 2010; Rossetti et al., 2010, 2013). In this scenario, the post-kinematic Ca-metasomatism affecting the base of the Alpine tectono-metamorphic pile of the Alboran Domain in the Rif documented in this study can be explained as caused by the structurally-controlled fluid-rock interaction and hydrothermal alteration processes (e.g. Mark & Foster 2000; Rose & Bird, 1994) associated with the early Miocene magmatism. We therefore propose that the post-tectonic growth of And, post-dating the composite Alpine fabric in the Alpujarride-Sebtide realm, is the response to a perturbed geothermal condition that affected an already structured nappe pile in response to a change in the geodynamic environment at regional scale during the early Miocene. This major change corresponds to the transition from orogenic construction to collapse in the region, during formation of the Alboran back-arc basin (e.g., Booth Rea et al., 2007; Comas et al., 1999; Dewey, 1988; Faccenna et al., 2004; García-Dueñas et al., 1992; Platt & Vissers, 1989; Vergés & Fernàndez, 2012; van Hinsbergen et al., 2020; Williams & Platt, 2018). Therefore, the ductile tectonic coupling between upper and lower Sebtides in the Alboran Domain in the Rif was already concluded before the early Miocene, pre-dating transition from orogenic construction to collapse in the Western Mediterranean region.

Still highly debated is the paleotectonic scenario that controlled the tectono-metamorphic evolution of the Alboran Domain during the Alpine orogeny, either referred to the south-dipping ("Alpine") or to the north-dipping ("Apennine-Maghrebian") subduction scenario (e.g., Carminati et al., 2012; Chalouan et al., 2008; Doglioni et al., 1999; Faccenna et al., 2001, 2004; Handy et al., 2010; Jolivet & Faccenna, 2009; Lacombe & Jolivet, 2005; Malusà et al., 2015; Michard et al., 2006; Molli & Malavieille, 2011; Platt et al., 2013; van Hinsbergen et al., 2020; Vérges & Fernàndez, 2012; Williams & Platt, 2018; Zeck, 1997). In this regard, the proposed Oligocene-Eocene to early Miocene timing for the Alpine metamorphism of the Alboran Domain (i) is consistent with the age of the orogenic metamorphism as recorded in oceanic- and continental-derived units in the hinterland of the Maghrebian-Apennine orogen, as documented in the Apennine-Tyrrhenian system (Calabria: ca. 45-35 Ma, Brandt & Schenk, 2020; Heymes et al., 2010; Rossetti et al., 2001a; Rossetti, Goffé, Monié, Faccenna, & Vignaroli, 2004; Schenk, 1980; Tuscany: ca. 27-16 Ma, Brunet, Monié, Jolivet, & Cadet, 2000; Kligfield, Hunziker, Dallmeyer, & Schamel, 1986; Rossetti et al., 2001b; Corsica: ca. 45-20 Ma, Beaudoin, Scaillet, Mora, Jolivet, & Augier, 2020; Brunet et al., 2000; Di Vincenzo, Grande, Prosser, Cavazza, & DeCelles, 2016; Rossetti, Glodny, Theye, & Maggi, 2015; Vitale Brovarone & Herwatz, 2013), and the Eastern Kabylia (ca. 32-21 Ma; Bruguier et al., 2017); and (ii) overlaps with the Oligocene-Miocene opening of the Liguro–Provençal and Tyrrhenian basins at the back of the eastward retreating Apennine-Maghrebian subduction front (e.g., Doglioni, Gueguen, Sàbat, & Fernandez, 1997; Faccenna et al., 2001; Gattacceca et al., 2007; Jolivet & Faccenna, 2000; Lacombe & Jolivet, 2005; Malinverno & Ryan, 1986; Rosenbaum et al., 2002; Royden, 1993; Séranne et al., 1999) (Figure

1a). This correlation allows us to frame the H*P* metamorphism of the Alboran Domain within a Cenozoic subduction channel formed along the convergent margin that accommodated the subduction of the Ligurian branch of the Tethyan realm below the European plate. We also infer that (i) the majority of the exhumation path of the H*P* units of the Alboran Domain occurred within the subduction channel, likely controlled by continuous underthrusting at depth, in a scenario dominated by continuous convergence (syn-orogenic exhumation; Figure 12a); and (ii) the syn-metamorphic exhumation of the Alpujarride-Sebtide Complex was nearly complete at ca. 22-21 Ma, when the H*P* units reached shallow crustal conditions and were finally exhumed under dominantly brittle environments, providing the source for the early Miocene syn-rift sedimentation (Lonergan & Mange-Rajetzky, 1994; Serrano et al, 2006). The progressive retreat of the Apennine-Maghrebian subduction system has therefore guided the transition from orogenic construction to collapse in the hinterland domain of the Betic-Rif orogen during formation of the Alboran basin, from early Miocene onward. This geodynamic event is recorded in the Western Mediterranean by the early Miocene transition from low- to high-*T* paleo-geothermal gradients and acidic magmatism of the same age in the exhumed metamorphic units of the Alboran Domain (Figure 12b).

## 9. CONCLUSION

The main results that can be extracted from this study are as follows:

(i) A polyphase Alpine metamorphic evolution is preserved in the H*P* aluminum silicate-quartz veins preserved as bounding within the retrogressive foliation of the BM1 unit of the Alboran Domain in the Moroccan Rif;

(ii) A minimum late Oligocene age can be proposed for the Alpine H*P* $D_1/M_1$ tectono-metamorphic stage in the Rif belt, suggesting as feasible the previously proposed Eocene timing for the subduction-zone metamorphism of the Alboran Domain

(iii) Exhumation is constrained by the continuous re-equilibration of the Wm composition (from high to low celadonite) from ca. 29 to 22 Ma, describing a nearly isothermal retrogressive path, with final re-equilibration at H*T*-L*T* conditions within the andalusite stability field.

(iv) Conclusive evidence is provided to link the early Miocene tectono-metamorphic event to a late thermal perturbation that affected the Alboran Domain at shallow crustal conditions, post-dating the almost complete exhumation of the deep roots of the Alpine belt in the Western Mediterranean.

(v) At regional scale, we suggest that the subduction-zone (H*P*/L*T*) metamorphism recorded in the Alboran Domain can be framed within the geodynamic scenario of the Apennine-Maghrebian subduction system from Eocene onward.

**ACKNOWLEDGEMENTS**

The authors wish to thank Arthur Iemmolo for the assistance during the Ar-Ar analyses. Moritz Schmeltz is thanked for sample preparation. The Grant to Department of Science, Roma Tre University (MIUR-Italy Dipartimenti di Eccellenza, ARTICOLO 958 1, COMMI 314-337 LEGGE 232/2016) is gratefully acknowledged. Figure 1a was produced with the GMT software package (Wessel et al., 2013). Constructive reviews and comments from the journal Editor K. Evans, M. Malusà and L. Jolivet contribute to improve the manuscript.

**REFERENCES**

Acosta-Vigil, A., Rubatto, D., Bartoli, O., Cesare, B., Meli, S., Pedrera, A., … Tajčmanová, L. (2014). Age of anatexis in the crustal footwall of the Ronda peridotites, S Spain. *Lithos*, *210–211*, 147–167. https://doi.org/10.1016/j.lithos.2014.08.018

Agard, P., Monié, P., Jolivet, L., & Goffé, B. (2002). Exhumation of the Schistes Lustrés complex: In situ laser probe 40Ar/39Ar constraints and implications for the Western Alps. *Journal of Metamorphic Geology*, *20*(6), 599–618. https://doi.org/10.1046/j.1525-1314.2002.00391.x

Agard, P., Plunder, A., Angiboust, S., Bonnet, G., & Ruh, J. (2018). The subduction plate interface: rock record and mechanical coupling (from long to short timescales). *Lithos*, *320–321*, 537–566. https://doi.org/10.1016/j.lithos.2018.09.029

Allaz, J., Engi, M., Berger, A., & Villa, I. M. (2011). The effects of retrograde reactions and of diffusion on $^{40}Ar$-$^{39}Ar$ ages of micas. *Journal of Petrology*, 52(4), 691–716. https://doi.org/10.1093/petrology/egq100

Álvarez-Valero, A. M., Jagoutz, O., Stanley, J., Manthei, C., Maz, A. El, Moukadiri, A., & Piasecki, A. (2014). Crustal attenuation as a tracer for the emplacement of the Beni Bousera ultramafic massif (Betico-Rifean belt). *Bulletin of the Geological Society of America*, *126*(11–12), 1614–1624. https://doi.org/10.1130/B31040.1

Andriessen, P. A. M., & Zeck, H. P. (1996). Fission-track constraints on timing of Alpine nappe emplacement and rates of cooling and exhumation, Torrox area, Betic Cordilleras, S. Spain. *Chemical Geology*, *131*(1–4), 199–206. https://doi.org/10.1016/0009-2541(95)00148-4

Augier, R., Agard, P., Monié, P., Jolivet, L., Robin, C., & Booth-Rea, G. (2005). Exhumation, doming and slab retreat in the Betic Cordillera (SE Spain): In situ $^{40}Ar/^{39}ar$ ages and P-T-d-t paths for the Nevado-Filabride complex. *Journal of Metamorphic Geology*, *23*(5), 357–381. https://doi.org/10.1111/j.1525-1314.2005.00581.x

Azañón, J. M., García-Dueñas, V., & Goffé, B. (1998). Exhumation of high-pressure metapelites and coeval crustal extension in the Alpujarride complex (Betic Cordillera). *Tectonophysics*, *285*(3–4), 231–252. https://doi.org/10.1016/S0040-1951(97)00273-4

Azañón, J. M., & Crespo-Blanc, A. (2000). Exhumation during a continental collision inferred from the tectonometamorphic evolution of the Alpujarride Complex in the central Betics (Alboran Domain, SE Spain). *Tectonics*, *19*(3), 549–565. https://doi.org/10.1029/2000TC900005

Azdimousa, A., Bourgois, J., Poupeau, G., Vázquez, M., Asebriy, L., & Labrin, E. (2014). Fission track thermochronology of the Beni Bousera peridotite massif (Internal Rif, Morocco) and the exhumation of ultramafic rocks in the Gibraltar Arc. *Arabian Journal of Geosciences*, *7*(5), 1993–2005. https://doi.org/10.1007/s12517-013-0924-3

Beaudoin, A., Scaillet, S., Mora, N., Jolivet, L., & Augier, R. (2020). In situ and step-heating 40Ar/39Ar dating of white mica in low-temperature shear zones (Tenda Massif, alpine Corsica, France). *Tectonics*, 39(12) e2020TC006246. https://doi.org/10.1029/2020TC006246

Bebout, G. E. (2014). *Chemical and Isotopic Cycling in Subduction Zones*. *Treatise on Geochemistry: Second Edition* (2nd ed., Vol. 15). Elsevier Ltd. https://doi.org/10.1016/B978-0-08-095975-7.01401-7

Booth-Rea, G., Azanón, J. M., Martínez-Martínez, J. M., Vidal, O., & García-Dueñas, V. (2005). Contrasting structural and P-T evolution of tectonic units in the southeastern Betics: Key for understanding the exhumation of the Alboran Domain HP/LT crustal rocks (western Mediterranean). *Tectonics*, *24*(2), 1–23. https://doi.org/10.1029/2004TC001640

Booth-Rea, G., Ranero, C. R., Martínez-Martínez, J. M., & Grevemeyer, I. (2007). Crustal types and tertiary tectonic evolution of the Alborán sea, western Mediterranean. *Geochemistry, Geophysics, Geosystems*, *8*(10), 1–25. https://doi.org/10.1029/2007GC001639

Bouybaouene, M. L., Goffé, B., & Michard, A. (1995). High-pressure, low-temperature metamorphism in the Sebtides nappes, northern Rif, Morocco. *Geogaceta*, 17, 117-119

Bouybaouenne, M., Michard, A., & Goffé, B. (1998). High-pressure granulites on top of the Beni Bousera peridotites, Rif belt, Morocco: a record of an ancient thickened crust in the Alboran domain. *Bull. Soc. Géol. France, 169*(2) 153-162

Brandt, S., & Schenk, V. (2020). Metamorphic response to Alpine thrusting of a crustal-scale basement nappe in southern Calabria (Italy). *Journal of Petrology.* https://doi.org/10.1093/petrology/egaa063

Bruguier, O., Bosch, D., Caby, R., Vitale-Brovarone, A., Fernandez, L., Hammor, D., ... & Mechati, M. (2017). Age of UHP metamorphism in the Western Mediterranean: insight from rutile and minute zircon inclusions in a diamond-bearing garnet megacryst (Edough Massif, NE Algeria). *Earth and Planetary Science Letters, 474*, 215-225. https://doi.org/10.1016/j.epsl.2017.06.043

Brunet, C., Monié, P., Jolivet, L., & Cadet, J. P. (2000). Migration of compression and extension in the Tyrrhenian Sea, insights from 40Ar/39Ar ages on micas along a transect from Corsica to Tuscany. *Tectonophysics*, 321(1), 127-155. https://doi.org/10.1016/S0040-1951(00)00067-6

Cao, S., Neubauer, F., Bernroider, M., & Genser, J. (2018). Eocene high-pressure metamorphism and Oligocene retrogression on Naxos, Cyclades, Greece: Significance for Aegean tectonics and 40Ar/39Ar dating in polyphase metamorphic rocks. *Tectonophysics*, *745*(August), 66–94. https://doi.org/10.1016/j.tecto.2018.08.009

Carminati, E., Lustrino, M., & Doglioni, C. (2012). Geodynamic evolution of the central and western Mediterranean: Tectonics vs. igneous petrology constraints. *Tectonophysics, 579*, 173-192. https://doi.org/10.1016/j.tecto.2012.01.026

Chalouan, A., & Michard, A. (2004). The Alpine Rif Belt (Morocco): A Case of Mountain Building in a Subduction-Subduction-Transform Fault Triple Junction. *Pure and Applied Geophysics* (Vol. 161). https://doi.org/10.1007/s00024-003-2460-7

Chalouan, A., Michard, A., El Kadiri, K., Negro, F., Frizon de Lamotte, D., Soto, J. I., & Saddiqi, O. (2008). The Rif Belt. *Lecture Notes in Earth Sciences*. https://doi.org/10.1007/978-3-540-77076-3_5

Comas, M. C., Platt, J. P., Soto, J. I., & Watts, A. B. (1999). The origin and tectonic history of the Alboran Basin: Insights from Leg 161 results. *Proceedings of the Ocean Drilling Program: Scientific Results*, *161*, 555–580. https://doi.org/10.2973/odp.proc.sr.161.262.1999

Connolly, J. A. D. (2005). Computation of phase equilibria by linear programming: A tool for geodynamic modeling and its application to subduction zone decarbonation. *Earth and Planetary Science Letters*, *236*(1–2), 524–541. https://doi.org/10.1016/j.epsl.2005.04.033

Dewey, J. F. (1988). Extensional collapse of orogens. *Tectonics*, *7*(6), 1123–1139. https://doi.org/10.1029/TC007i006p01123

Di Vincenzo, G., Carosi, R., Palmeri, R. (2004). The Relationship between Tectono-metamorphic Evolution and Argon Isotope Records in White Mica: Constraints from in situ 40Ar-39Ar Laser Analysis of the Variscan Basement of Sardinia. *Journal of Petrology*, *45*(5), 1013–1043. https://doi.org/10.1093/petrology/egh002

Di Vincenzo, G., Tonarini, S., Lombardo, B., Castelli, D., & Ottolini, L. (2006). Comparison of 40Ar-39Ar and Rb-Sr data on phengites from the UHP Brossasco-Isasca unit (Dora Maira Massif, Italy): Implications for dating white Mica. *Journal of Petrology*, *47*(7), 1439–1465. https://doi.org/10.1093/petrology/egl018

Di Vincenzo, G., Grande, A., Prosser, G., Cavazza, W., & DeCelles, P. G. (2016). $^{40}$Ar–$^{39}$Ar laser dating of ductile shear zones from central Corsica (France): evidence of Alpine (middle to late Eocene) syn-burial shearing in Variscan granitoids. *Lithos*, 262, 369-383. https://doi.org/10.1016/j.lithos.2016.07.022

Doglioni, C., Gueguen, E., Sàbat, F., & Fernandez, M. (1997). The western Mediterranean extensional basins and the Alpine orogen. *Terra Nova, 9*(3), 109-112. https://doi.org/10.1046/j.1365-3121.1997.d01-18.x

Doglioni, C., Gueguen, E., Harabaglia, P., & Mongelli, F. (1999). On the origin of west-directed subduction zones and applications to the western Mediterranean. *Geological Society, London, Special Publications, 156*(1), 541-561. https://doi.org/10.1144/GSL.SP.1999.156.01.24

Durand-Delga, M., Feinberg, H., Magné, J., Olivier, P., & Anglada, R. (1993). Les formations oligo-miocènes discordantes sur les Malaguides et les Alpujarrides et leurs implications dans l'évolution géodynamique des Cordillères Bétiques (Espagne) et de la Mediterranée d'Alboran. *Comptes Rendus de l'Académie Des Sciences. Série 2, Mécanique, Physique, Chimie, Sciences de l'univers, Sciences de La Terre*, *317*(5), 679–687.

El Maz, A., & Guiraud, M. (2001). Paragenese a faible variance dans les metapelites de la serie de Filali (Rif interne marocain): description, interpretation et consequence geodynamique. *Bull. Soc. Géol. France, 4,* 469-485. https://doi.org/https://doi.org/10.2113/172.4.469

Esteban, J. J., Cuevas, J., Tubía, J. M., Sergeev, S., & Larionov, A. (2010). A revised Aquitanian age for the emplacement of the Ronda peridotites (Betic Cordilleras, southern Spain). *Geological Magazine*, *148*(01), 183–187. https://doi.org/10.1017/S0016756810000737

Faccenna, C., Becker, T. W., Lucente, F. P., Jolivet, L., & Rossetti, F. (2001). History of subduction and back-arc extension in the central Mediterranean. *Geophysical Journal International*, *145*(3), 809–820. https://doi.org/10.1046/j.0956-540X.2001.01435.x

Faccenna, C., Piromallo, C., Crespo-Blanc, A., Jolivet, L., & Rossetti, F. (2004). Lateral slab deformation and the origin of the western Mediterranean arcs. *Tectonics*, *23*(1). https://doi.org/10.1029/2002TC001488

Faccenna, C., Becker, T. W., Auer, L., Billi, A., Boschi, L., Brun, J. P., … Serpelloni, E. (2014). Mantle dynamics in the Mediterranean. *American Geophysical Union*, *52*(3), 283–332. https://doi.org/10.1002/2013RG000444

Frasca, G., Gueydan, F., Poujol, M., Brun, J. P., Parat, F., Monié, P., … Mazier, S. (2017). Fast switch from extensional exhumation to thrusting of the Ronda Peridotites (South Spain). *Terra Nova*, *29*(2), 117–126. https://doi.org/10.1111/ter.12255

García-Dueñas, V., Balanyá, J. C., & Martínez-Martínez, J. M. (1992). Miocene extensional detachments in the outcropping basement of the northern Alboran Basin (Betics) and their tectonic implications. *Geo-Marine Letters*, *12*(2–3), 88–95. https://doi.org/10.1007/BF02084917

Garrido, C. J., Gueydan, F., Booth-Rea, G., Precigout, J., Hidas, K., Padrón-Navarta, J. A. & Marchesi, C. (2011). Garnet lherzolite and garnet-spinel mylonite in the Ronda peridotite: Vestiges of Oligocene backarc mantle lithospheric extension in the western Mediterranean. *Geology, 39*(10), 927–930. doi:10.1130/G31760.1;

Gattacceca, J., Deino, A., Rizzo, R., Jones, D. S., Henry, B., Beaudoin, B., & Vadeboin, F. (2007). Miocene rotation of Sardinia: New paleomagnetic and geochronological constraints and geodynamic implications. *Earth and Planetary Science Letters, 258*(3-4), 359-377. https://doi.org/10.1016/j.epsl.2007.02.003

Goffe, B., Azañón, J. M., Bouybaouene, M. L., & Jullien, M. (1996). Metamorphic cookeite in Alpine metapelites from Rif, northern Morocco, and the Betic Chain, southern Spain. *European Journal of Mineralogy-Ohne Beihefte,* *8*(2), 335-348. https://doi.org/10.1127/ejm/8/2/0335

Guerrera, F., Martín-Martín, M., & Tramontana, M. (2019). Evolutionary geological models of the central-western peri-Mediterranean chains: a review. *International Geology Review*, *00*(00), 1–22. https://doi.org/10.1080/00206814.2019.1706056

Gueydan, F., Pitra, P., Afiri, A., Poujol, M., Essaifi, A., & Paquette, J. L. (2015). Oligo-Miocene thinning of the Beni Bousera peridotites and their Variscan crustal host rocks, Internal Rif, Morocco. *Tectonics*, *34*(6), 1244–1268. https://doi.org/10.1002/2014TC003769

Gueydan, F., Mazzotti, S., Tiberi, C., Cavin, R., & Villaseñor, A. (2019). Western Mediterranean subcontinental mantle emplacement by continental margin obduction. *Tectonics*, *38*(6), 2142–2157. https://doi.org/10.1029/2018TC005058

Handy, M. R., Schmid, S. M., Bousquet, R., Kissling, E., & Bernoulli, D. (2010). Reconciling plate-tectonic reconstructions of Alpine Tethys with the geological–geophysical record of spreading and subduction in the Alps. *Earth-Science Reviews*, 102(3-4), 121-158. https://doi.org/10.1016/j.earscirev.2010.06.002

Harrison, T. M., Célérier, J., Aikman, A. B., Hermann, J., & Heizler, M. T. (2009). Diffusion of 40Ar in muscovite. *Geochimica et Cosmochimica Acta*, *73*(4), 1039–1051. https://doi.org/10.1016/j.gca.2008.09.038

Herwegh, M., Berger, A., Glotzbach, C., Wangenheim, C., Mock, S., Wehrens, P., ... & Kissling, E. (2020). Late stages of continent-continent collision: Timing, kinematic evolution, and exhumation of the Northern rim (Aar Massif) of the Alps. *Earth-science reviews*, 200, 102959. https://doi.org/10.1016/j.earscirev.2019.102959

Heymes, T., Monié, P., Arnaud, N., Pêcher, A., Bouillin, J. P., & Compagnoni, R. (2010). Alpine tectonics in the Calabrian–Peloritan belt (southern Italy): New $^{40}Ar/^{39}Ar$ data in the Aspromonte Massif area. *Lithos*, 114(3-4), 451-472. https://doi.org/10.1016/j.lithos.2009.10.011

Hidas, K., Booth-Rea, G., Garrido, C. J., Martínez-Martínez, J. M., Padrón-Navarta, J. A., Konc, Z., … Marchesi, C. (2013). Backarc basin inversion and subcontinental mantle emplacement in the crust: kilometre-scale folding and shearing at the base of the proto-Alborán lithospheric mantle (Betic Cordillera, southern Spain). *Journal of the Geological Society*, *170*(1), 47–55. https://doi.org/10.1144/jgs2011-151

Holland, T., & Powell, R. (2004). An internally consistent thermodynamic data set for phases of petrological interest. *Journal of Metamorphic Geology*, *16*(3), 309–343. https://doi.org/10.1111/j.1525-1314.1998.00140.x

Homonnay, E., Corsini, M., Lardeaux, J. M., Romagny, A., Münch, P., Bosch, D., … Ouazzani-Touhami, M. (2018). Miocene crustal extension following thrust tectonic in the Lower Sebtides units (internal Rif, Ceuta Peninsula, Spain): Implication for the geodynamic evolution of the Alboran domain. *Tectonophysics*, *722*(November 2017), 507–535.

https://doi.org/10.1016/j.tecto.2017.11.028

Janots, E., Negro, F., Brunet, F., Goffé, B., Engi, M., & Bouybaouène, M. L. (2006). Evolution of the REE mineralogy in HP-LT metapelites of the Sebtide complex, Rif, Morocco: Monazite stability and geochronology. *Lithos*, *87*(3–4), 214–234. https://doi.org/10.1016/j.lithos.2005.06.008

Jolivet, L., & Faccenna, C. (2000). Mediterranean extension and the Africa-Eurasia collision. *Tectonics*, 19(6), 1095–1106. https://doi.org/10.1029/2000TC900018

Jolivet, L., Faccenna, C., Goffé, B., Burov, E., & Agard, P. (2003). Subduction tectonics and exhumation of high-pressure metamorphic rocks in the Mediterranean orogens. *American Journal of Science*, *303*(5), 353–409. https://doi.org/10.2475/ajs.303.5.353

Jolivet, L., Augier, R., Faccenna, C., Negro, F., Rimmele, G., Agard, P., … Crespo-Blanc, A. (2008). Subduction, convergence and the mode of backarc extension in the Mediterranean region. *Bulletin de La Societe Geologique de France*, *179*(6), 525–550. https://doi.org/10.2113/gssgfbull.179.6.525

Kligfield, R., Hunziker, J., Dallmeyer, R. D., & Schamel, S. (1986). Dating of deformation phases using K-Ar and $^{40}Ar/^{39}Ar$ techniques: results from the Northern Apennines. *Journal of Structural Geology, 8*(7), 781-798. https://doi.org/10.1016/0191-8141(86)90025-8

Kornprobst, J. (1974). Contribution a l'ètude pètrographique et structurale de la zone interne du Rif (Maroc septentrional); Petrography and structure of the Rif inner area, northern Morocco. *Notes Mèm. Serv. Gèol. Rabat*, *251*, 256.

Lacombe, O., & Jolivet, L. (2005). Structural and kinematic relationships between Corsica and the Pyrenees-Provence domain at the time of the Pyrenean orogeny. *Tectonics*, 24(1). https://doi.org/10.1029/2004TC001673

Laurent, V., Huet, B., Labrousse, L., Jolivet, L., Monié, P., & Augier, R. (2017). Extraneous argon in high-pressure metamorphic rocks: Distribution, origin and transport in the Cycladic Blueschist Unit (Greece). *Lithos*, *272–273*, 315–335. https://doi.org/10.1016/j.lithos.2016.12.013

Law, R. D. (2014). Deformation thermometry based on quartz c-axis fabrics and recrystallization microstructures: A review. *Journal of Structural Geology*, *66*, 129–161. https://doi.org/10.1016/j.jsg.2014.05.023

Li, B., & Massonne, H. J. (2018). Two Tertiary metamorphic events recognized in high-pressure metapelites of the Nevado-Filábride Complex (Betic Cordillera, S Spain). *Journal of Metamorphic Geology*, *36*(5), 603–630. https://doi.org/10.1111/jmg.12312

Lonergan, L. (1993). Timing and kinematics of deformation in the Malaguide Complex, internal zone of the Betic Cordillera, southeast Spain. *Tectonics*, *12*(2), 460–476. https://doi.org/https://doi.org/10.1029/92TC02507

Lonergan, L., & Mange-Rajetzky, M. A. (1994). Evidence for Internal Zone unroofing from foreland basin sediments, Betic Cordillera, SE Spain. *Journal of the Geological Society (London)*, *151*, 515–529. https://doi.org/10.1144/gsjgs.151.3.0515

Lonergan, L., & Johnson, C. (1998). A novel approach for reconstructing the denudation histories of mountain belts: with an example from the Betic Cordillera (S. Spain). *Basin Research*, *10*, 353–364.

Loomis, T. P. (1975). Tertiary mantle diapirism, orogeny, and plate tectonics east of the Strait of Gibraltar. *American Journal of Science, 275*(1), 1-30. https://doi.org/10.2475/ajs.275.1.1

Maggi, M., Rossetti, F., Corfu, F., Theye, T., Andersen, T. B., & Faccenna, C. (2012). Clinopyroxene–rutile phyllonites from the East Tenda Shear Zone (Alpine Corsica, France): pressure–temperature–time constraints to the Alpine reworking of Variscan Corsica. *Journal of the Geological Society*, 169(6), 723-732. https://doi.org/10.1144/jgs2011-120

Malinverno, A., & Ryan, W. B. (1986). Extension in the Tyrrhenian Sea and shortening in the Apennines as result of arc migration driven by sinking of the lithosphere. *Tectonics, 5*(2), 227-245. https://doi.org/10.1029/TC005i002p00227

Malusà, M. G., Faccenna, C., Baldwin, S. L., Fitzgerald, P. G., Rossetti, F., Danisik, M., … Piromallo, C. (2015). Contrasting styles of (U)HP rock exhumation along the Cenozoic Adria-Europe plate boundary (Western Alps, Calabria, Corsica). *Geochemistry, Geophysics, Geosystems*, 1786–1824. https://doi.org/10.1002/2015GC005767

Mark, G., & Foster, D. R. W. (2000). Magmatic–hydrothermal albite–actinolite–apatite-rich rocks from the Cloncurry district. *Lithos*, *51*, 223–245. https://doi.org/https://doi.org/10.1016/S0024-4937(99)00069-9

Martínez-Martínez, J. M., Soto, J. I., & Balanyá, J. C. (2002). Orthogonal folding of extensional detachments: Structure and origin of the Sierra Nevada elongated dome (Betics, SE Spain). *Tectonics*, *21*(3), 3-1-3–20. https://doi.org/10.1029/2001TC001283

Maruyama, S., Liou, J. G., & Terabayashi, M. (1996). Blueschists and eclogites of the world and their exhumation. *International Geology Review*, *38*(6), 485–594. https://doi.org/10.1080/00206819709465347

Massonne, H. J. (2014). Wealth of P–T–t information in medium-high grade metapelites: Example from the Jubrique Unit of the Betic Cordillera, S Spain. *Lithos*, 208, 137-157. https://doi.org/10.1016/j.lithos.2014.08.027

Mazzoli, S., & Martín-Algarra, A. (2011). Deformation partitioning during transpressional emplacement of a 'mantle extrusion wedge': the Ronda peridotites, western Betic Cordillera, Spain. *Journal of the Geological Society, 168*(2), 373-382. https://doi.org/10.1144/0016-76492010-126

Mazzoli, S., Martín-Algarra, A., Reddy, S. M., Sánchez-Vizcaíno, V. L., Fedele, L., & Noviello, A. (2013). The evolution of the footwall to the Ronda subcontinental mantle peridotites: Insights from the Nieves unit (western Betic Cordillera). *Journal of the Geological Society*, *170*(3), 385–402. https://doi.org/10.1144/jgs2012-105

Melchiorre, M., Álvarez-Valero, A. M., Vergés, J., Fernàndez, M., Belousova, E. A., El Maz, A., & Moukadiri, A. (2017). In situ U-Pb zircon geochronology on metapelitic granulites of Beni Bousera (Betic-Rif system, N Morocco). *Special Paper of the Geological Society of America*, *526*(08), 151–171. https://doi.org/10.1130/2017.2526(08)

Michard, A., Goffé, B., Bouybaouene, M. L., & Saddiqi, O. (1997). Late Hercynian-Mesozoic thinning in the Alboran domain: Metamorphic data from the northern Rif, Morocco. *Terra Nova*, *9*(4), 171–174. https://doi.org/10.1046/j.1365-3121.1997.d01-24.x

Michard, A., Chalouan, A., Feinberg, H., Goffé, B., & Montigny, R. (2002). How does the Alpine belt end between Spain and Morocco?. *Bulletin de la Société géologique de France, 173*(1), 3-15. https://doi.org/10.3749/canmin.48.1.183

Michard, A., Negro, F., Saddiqi, O., Bouybaouene, M. L., Chalouan, A., Montigny, R., & Goffé, B. (2006). Pressure-temperature-time constraints on the Maghrebide mountain building: Evidence from the Rif-Betic transect (Morocco, Spain), Algerian correlations, and geodynamic implications. *Comptes Rendus - Geoscience*, *338*(1–2), 92–114. https://doi.org/10.1016/j.crte.2005.11.011

Molli, G., & Malavieille, J. (2011). Orogenic processes and the Corsica/Apennines geodynamic evolution: insights from Taiwan. *International Journal of Earth Sciences*, 100(5), 1207-1224.

https://doi.org/10.1007/s00531-010-0598-y

Monié, P., Galindo-Zaldivar, J., Lodeiro, F. G., Goffé, B., & Jabaloy, A. (1991). $^{40}$Ar/$^{39}$Ar geochronology of Alpine tectonism in the Betic Cordilleras (southern Spain). *Journal of the Geological Society, 148*(2), 289-297. https://doi.org/10.1144/gsjgs.148.2.0289

Monié, P., Torres-Roldán, R. L., & García-Casco, A. (1994). Cooling and exhumation of the Western Betic Cordilleras, 40Ar/39Ar thermochronological constraints on a collapsed terrane. *Tectonophysics*, *238*(1–4), 353–379. https://doi.org/10.1016/0040-1951(94)90064-7

Monié, P., & Agard, P. (2009). Coeval blueschist exhumation along thousands of kilometers: Implications for subduction channel processes. *Geochemistry, Geophysics, Geosystems*, *10*(7). https://doi.org/10.1029/2009GC002428

Montel, J. M., Kornprobst, J., & Vielzeuf, D. (2000). Preservation of old U-Th-Pb ages in shielded monazite: Example from the Beni Bousera Hercynian kinzigites (Morocco). *Journal of Metamorphic Geology*, *18*(3), 335–342. https://doi.org/10.1046/j.1525-1314.2000.00261.x

Negro, F., Beyssac, O., Goffé, B., Saddiqi, O., & Bouybaouène, M. L. (2006). Thermal structure of the Alboran Domain in the Rif (northern Morocco) and the Western Betics (southern Spain). Constraints from Raman spectroscopy of carbonaceous material. *Journal of Metamorphic Geology*, *24*(4), 309–327. https://doi.org/10.1111/j.1525-1314.2006.00639.x

Passchier, C.W., & Trouw, R. A. J. (2010). *Micro-tectonics*. Spriger.

Peacock, S. M. (1996). Thermal and petrologic structure of subduction zones. *Geophysical Monograph Series*, *96*, 119–133. https://doi.org/10.1029/GM096p0119

Pearson, D. G., Davies, G. R., & Nixon, P. H. (1993). Geochemical Constraints on the Petrogenesis of Diamond Fades Pyroxenites from the Beni Bousera Peridotite Massif, North Morocco. *Journal of Petrology*, *34*, 125–172. https://doi.org/10.1093/petrology/34.1.125

Penniston-Dorland, S. C., Kohn, M. J., & Manning, C. E. (2015). The global range of subduction zone thermal structures from exhumed blueschists and eclogites: Rocks are hotter than models. *Earth and Planetary Science Letters*, *428*, 243–254. https://doi.org/10.1016/j.epsl.2015.07.031

Platt, J. P., & Vissers, R. L. M. (1989). Extensional collapse of thickened continental lithosphere: a working hypothesis for the Alboran Sea and Gibraltar arc. *Geology*, *17*(6), 540–543. https://doi.org/10.1130/0091-7613(1989)017<0540:ECOTCL>2.3.CO;2

Platt, J. P., Soto, J., Whitehouse, M. J., Hurford, a J., Kelley, S. P., & Conrad, D. (1998). Thermal evolution, rate of exhumation, and tectonic significance of metamorphic rocks from the floor of the Alboran extensional basin, western Mediterranean. *Tectonics*, *17*(5), 671–689. https://doi.org/10.1029/98TC02204

Platt, J. P., & Whitehouse, M. J. (1999). Early Miocene high-temperature metamorphism and rapid exhumation in the Betic Cordillera (Spain): Evidence from U-Pb zircon ages. *Earth and Planetary Science Letters*, *171*(4), 591–605. https://doi.org/10.1016/S0012-821X(99)00176-4

Platt, J. P., Whitehouse, M. J., Kelley, S. P., Carter, A., & Hollick, L. (2003a). Simultaneous extensional exhumation across the Alboran Basin: Implications for the causes of late orogenic extension. *Geology*, *31*(3), 251–254. https://doi.org/10.1130/0091-7613(2003)031<0251:SEEATA>2.0.CO;2

Platt, J. P, Argles, T. W., Carter, A., Kelley, S. P., Whitehouse, M. J., & Lonergan, L. (2003b). Exhumation of the Ronda peridotite and its crustal envelope: constraints from thermal modelling of a P-T-time array. *Journal of the Geological Society*, *160*(5), 655–676. https://doi.org/10.1144/0016-764902-108

Platt, J. P., Allerton, S., Kirker, A., Mandeville, C., Mayfield, A., Platzman, E. S., & Rimi, A. (2003c). The ultimate arc: Differential displacement, oroclinal bending, and vertical axis rotation in the External Betic-Rif arc. *Tectonics*, *22*(3). https://doi.org/10.1029/2001TC001321

Platt, J. P., Kelley, S.P., Carter, A., Orozco, M. (2005). Timing of tectonic events in the Alpujarride Complex, Betic Cordillera, southern Spain, *162*, 451–462. https://doi.org/https://doi.org/10.1144/0016-764903-039

Platt, J. P., Anczkiewicz, R., Soto, J. I., Kelley, S. P., & Thirlwall, M. (2006). Early Miocene continental subduction and rapid exhumation in the western Mediterranean. *Geology*, *34*(11), 981–984. https://doi.org/10.1130/G22801A.1

Platt, J. P. (2007). From orogenic hinterlands to Mediterranean-style back-arc basins: A comparative analysis. *Journal of the Geological Society*, *164*(2), 297–311. https://doi.org/10.1144/0016-76492006-093

Platt, J. P., Behr, W. M., Johanesen, K., & Williams, J. R. (2013). The Betic-Rif Arc and Its Orogenic Hinterland: A Review. *Annual Review of Earth and Planetary Sciences*, *41*(1), 313–357. https://doi.org/10.1146/annurev-earth-050212-123951

Plunder, A., Agard, P., Chopin, C., Pourteau, A., & Okay, A. I. (2015). Accretion, underplating and exhumation along a subduction interface: From subduction initiation to continental subduction

(Tavşanli zone, W. Turkey). *Lithos*, *226*, 233–254. https://doi.org/10.1016/j.lithos.2015.01.007

Powell, R., & Holland, T. J. B. (2008). On thermobarometry. *Journal of Metamorphic Geology*, *26*(2), 155–179. https://doi.org/10.1111/j.1525-1314.2007.00756.x

Rodríguez-Ruiz, M. D., Abad, I., & Bentabol, M. J. (2019). Permo-triassic clastic rocks from the ghomaride complex and federico units (Rif Cordillera, N Morocco): An example of diagenetic-metamorphic transition. *Minerals*, *9*(12). https://doi.org/10.3390/min9120738

Romagny, A., Münch, P. H., Cornée, J. J., Corsini, M., Azdimousa, A., Melinte-Dobrinescu, M. C., … Ben Moussa, A. (2014). Late Miocene to present-day exhumation and uplift of the Internal Zone of the Rif chain: Insights from low temperature thermochronometry and basin analysis. *Journal of Geodynamics*, *77*, 39–55. https://doi.org/10.1016/j.jog.2014.01.006

Rose, N. M., & Bird, D. K. (1994). Hydrothermally altered dolerite dykes in East Greenland: *Contributions to Mineralogy and Petrology*, *116*, 420–432.

Rosenbaum, G., Lister, G. S., & Duboz, C. (2002). Reconstruction of the tectonic evolution of the western Mediterranean since the Oligocene. *Journal of the Virtual Explorer*, *8*(January). https://doi.org/10.3809/jvirtex.2002.00053

Rossetti, F., Faccenna, C., Goffé, B., Monié, P., Argentieri, A., Funiciello, R., & Mattei, M. (2001a). Alpine structural and metamorphic signature of the Sila Piccola Massif nappe stack (Calabria, Italy): Insights for the tectonic evolution of the Calabrian Arc. *Tectonics*, 20(1), 112-133. https://doi.org/10.1029/2000TC900027

Rossetti, F., Faccenna, C., Jolivet, L., Funiciello, R., Goffé, B., Tecce, F., ... & Vidal, O. (2001b). Structural signature and exhumation PTt path of the Gorgona blueschist sequence (Tuscan Archipelago, Italy). *Ofioliti*, 26(2a), 175-186.

Rossetti, F., Goffé, B., Monié, P., Faccenna, C., & Vignaroli, G. (2004). Alpine orogenic *P-T-t*-deformation history of the Catena Costiera area and surrounding regions (Calabrian Arc, southern Italy): The nappe edifice of north Calabria revised with insights on the Tyrrhenian-Apennine system formation. *Tectonics*, 23(6). https://doi.org/10.1029/2003TC001560

Rossetti, F., Faccenna, C., & Crespo-Blanc, A. (2005). Structural and kinematic constraints to the exhumation of the Alpujarride Complex (Central Betic Cordillera, Spain). *Journal of Structural Geology*, *27*(2), 199–216. https://doi.org/10.1016/j.jsg.2004.10.008

Rossetti, F., Theye, T., Lucci, F., Bouybaouene, M. L., Dini, A., Gerdes, A., … Cozzupoli, D. (2010). Timing and modes of granite magmatism in the core of the Alboran Domain, Rif chain, northern Morocco: Implications for the Alpine evolution of the western Mediterranean. *Tectonics*, *29*(2). https://doi.org/10.1029/2009TC002487

Rossetti, F., Dini, A., Lucci, F., Bouybaouenne, M., & Faccenna, C. (2013). Early Miocene strike-slip tectonics and granite emplacement in the Alboran Domain (Rif Chain, Morocco): significance for the geodynamic evolution of Western Mediterranean. *Tectonophysics*, *608*, 774–791. https://doi.org/10.1016/J.TECTO.2013.08.002

Rossetti, F., Glodny, J., Theye, T., & Maggi, M. (2015). Pressure–temperature–deformation–time of the ductile Alpine shearing in Corsica: From orogenic construction to collapse. *Lithos*, 218, 99-116. https://doi.org/10.1016/j.lithos.2015.01.011

Rossetti, F., Lucci, F., Theye, T., Bouybaouenne, M., Gerdes, A., Opitz, J., Lipp, C. (2020). Hercynian anatexis in the envelope of the Beni Bousera peridotites (Alboran Domain, Morocco): Implications for the tectono-metamorphic evolution of the deep crustal roots of the Mediterranean region. *Gondwana Research*, *83*, 157–182. https://doi.org/10.1016/j.gr.2020.01.020

Royden, L. H. (1993). Evolution of retreating subduction boundaries formed during continental collision. *Tectonics, 12*(3), 629-638. https://doi.org/10.1029/92TC02641

Ruiz Cruz, M. D., De Galdeano, C. S., Alvarez-Valero, A., Rodriguez Ruiz, M. D., & Novák, J. (2010). Pumpellyite and coexisting minerals in metapelites and veins from the federico units in the internal zone of the rif, Spain. *Canadian Mineralogist*, *48*(1), 183–203. https://doi.org/10.3749/canmin.48.1.183

Sánchez-Navas, A., García-Casco, A., Mazzoli, S., & Martín-Algarra, A. (2017). Polymetamorphism in the alpujarride complex, Betic Cordillera, South Spain. *Journal of Geology*, *125*(6), 637–657. https://doi.org/10.1086/693862

Sánchez-Rodríguez, L., & Gebauer, D. (2000). Mesozoic formation of pyroxenites and gabbros in the Ronda area (southern Spain), followed by Early Miocene subduction metamorphism and emplacement into the middle crust: U-Pb sensitive high-resolution ion microprobe dating of zircon. *Tectonophysics*, *316*(1–2), 19–44. https://doi.org/10.1016/S0040-1951(99)00256-5

Schenk, V. (1980). U-Pb and Rb-Sr radiometric dates and their correlation with metamorphic events in the granulite facies basement of the Serre, southern Calabria (Italy). *Contributions to*

*Mineralogy and Petrology, 73*, 23-38. https://doi.org/10.1007/BF00376258

Séranne, M. (1999). The Gulf of Lion continental margin (NW Mediterranean) revisited by IBS: an overview. *Geological Society, London, Special Publications*, 156(1), 15-36. https://doi.org/10.1144/GSL.SP.1999.156.01.03

Serrano, F., de Galdeano, C. S., El Kadiri, K., Guerra-Merchán, A., López-Garrido, A. C., Martín-Martín, M., & Hlila, R. (2006). Oligocene-early Miocene transgressive cover of the Betic-Rif Internal Zone. Revision of its geologic significance. *Eclogae Geologicae Helvetiae, 99*(2), 237-253. https://doi.org/10.1007/s00015-006-1186-9

Simancas, J. F., & Campos, J. (1993). Compresión NNW–SSE tardi a postmetamórfica y extensión subordinada en el Complejo Alpujárride (Dominio de Alborán, Orógeno Bético). *Rev. Soc. Geol. España*.

Stipp, M., Stünitz, H., Heilbronner, R., & Schmid, S. M. (2002). Dynamic recrystallization of quartz: Correlation between natural and experimental conditions. *Geological Society Special Publication*, *200*, 171–190. https://doi.org/10.1144/GSL.SP.2001.200.01.11

Taylor-Jones, K., & Powell, R. (2015). Interpreting zirconium-in-rutile thermometric results. *Journal of Metamorphic Geology*, *33*(2), 115–122. https://doi.org/10.1111/jmg.12109

Tomkins, H. S., Powell, R., & Ellis, D. J. (2007). The pressure dependence of the zirconium-in-rutile thermometer. *Journal of Metamorphic Geology*, *25*(6), 703–713. https://doi.org/10.1111/j.1525-1314.2007.00724.x

Tubía, J.M., & Cuevas, J. (1987). Structures et cinématique liées à la mise en place des péridotites de Ronda (Cordillères Bétiques, Espagne). *Geodinamica Acta*, *1*(1), 59–69. https://doi.org/https://doi.org/10.1080/09853111.1987.11105125

Tubía, J. M., Cuevas, J., & Esteban, J. J. (2004). Tectonic evidence in the Ronda peridotites, Spain, for mantle diapirism related to delamination. *Geology*, *32*(11), 941–944. https://doi.org/10.1130/G20869.1

Turner, S. P., Platt, J. P., George, R. M. M., Kelley, S. P., Pearson, D. G., & Nowell, G. M. (1999). Magmatism associated with orogenic collapse of the Betic-Alboran Domain, SE Spain. *Journal of Petrology*, *40*(6), 1011–1036. https://doi.org/10.1093/petroj/40.6.1011

Van der Wal, D., & Vissers, R. L. M. (1993). Uplift and emplacement of upper mantle rock in the western Mediterranean, *21(12)*, 1119–1122. https://doi.org/https://doi.org/10.1130/0091-

7613(1993)021<1119:UAEOUM>2.3.CO;2

van Hinsbergen, D. J. J., Vissers, R. L. M., & Spakman, W. (2014). Origin and consequences of western Mediterranean subduction, rollback, and slab segmentation. *Tectonics*. https://doi.org/10.1002/2013TC003349

van Hinsbergen, D. J., Torsvik, T. H., Schmid, S. M., Maţenco, L. C., Maffione, M., Vissers, R. L., ... & Spakman, W. (2020). Orogenic architecture of the Mediterranean region and kinematic reconstruction of its tectonic evolution since the Triassic. *Gondwana Research*, 81, 79-229. https://doi.org/10.1016/j.gr.2019.07.009

Vergés, J., & Fernàndez, M. (2012). Tethys-Atlantic interaction along the Iberia-Africa plate boundary: The Betic-Rif orogenic system. *Tectonophysics*, *579*, 144–172. https://doi.org/10.1016/j.tecto.2012.08.032

Vidal, O., Goffé, B., Bousquet, R., & Parra, T. (1999). Calibration and testing of an empirical chloritoid-chlorite Mg-Fe exchange thermometer and thermodynamic data for daphnite. *Journal of Metamorphic Geology*, *17*(1), 25–39. https://doi.org/10.1046/j.1525-1314.1999.00174.x

Villa, I. M. (2010). Disequilibrium textures versus equilibrium modelling: Geochronology at the crossroads. *Geological Society Special Publication*, *332*, 1–15. https://doi.org/10.1144/SP332.1

Villa, I. M. (2016). Diffusion in mineral geochronometers: Present and absent. *Chemical Geology*, *420*, 1–10. https://doi.org/10.1016/j.chemgeo.2015.11.001

Vitale Brovarone, A., & Herwartz, D. (2013). Timing of HP metamorphism in the Schistes Lustrés of Alpine Corsica: New Lu–Hf garnet and lawsonite ages. *Lithos*, 172, 175-191. https://doi.org/10.1016/j.lithos.2013.03.009

Wessel, P., Smith, W.H.F., Scharroo, R., Luis, J., Wobbe, F. (2013). Generic mapping tools: improved version released. *Eos, Trans. Am. Geophys. Union* 94, 409–410. https://doi.org/10.1002 /2013EO450001.

Whitney, D. L., & Evans, B. W. (2010). Abbreviations for names of rock-forming minerals. *American Mineralogist*, *95*(1), 185–187. https://doi.org/10.2138/am.2010.3371

Williams, J. R., & Platt, J. P. (2018). A new structural and kinematic framework for the Alborán Domain (Betic–Rif arc, western Mediterranean orogenic system). *Journal of the Geological*

*Society, 175*(3), 465-496. https://doi.org/10.1144/jgs2017-086platt

Zaghloul, M. N. (1994). Les Unités Federico septentrionales (Rif interne, Maroc): Inventaire des deformations et leur contexte géodynamique dans la cha ne Bético–Rifaine. *Thèse de 3ème Cycle*, *Université*, 218.

Zeck, H. P., Monie, P., Villa, I. M., & Hansen B. T. (1992). Very High-Rates of Cooling and Uplift in the Alpine Belt of the Betic Cordilleras, Southern Spain. *Geology*, *20*(11), 1053–1054. https://doi.org/10.1130/0091-7613(1992)020<0079:VHROCA>2.3.CO;2

Zeck, H. P. (1996). Betic-Rif orogeny: Subduction of Mesozoic Tethys lithosphere under eastward drifting Iberia, slab detachment shortly before 22 Ma, and subsequent uplift and extensional tectonics. *Tectonophysics*, *254*(1–2), 1–16. https://doi.org/10.1016/0040-1951(95)00206-5

Zeck, H. P. (1997). Mantle peridotites outlining the Gibraltar Arc - Centrifugal extensional allochthons derived from the earlier Alpine, westward subducted nappe pile. *Tectonophysics*, *281*(3–4), 195–207. https://doi.org/10.1016/S0040-1951(97)00067-X

Zeck, H. P., & Whitehouse, M. J. (1999). Hercynian, Pan-African, Proterozoic and Archean ion-microprobe zircon ages for a Betic-Rif core complex, Alpine belt, W Mediterranean-consequences for its P-T-t path. *Contributions to Mineralogy and Petrology*, *134*, 134–149. https://doi.org/10.1007/s004100050474

Zeck, H. P., & Williams, I. S. (2001). Hercynian Metamorphism in Nappe Core Complexes of the Alpine Betic-Rif Belt, Western Mediterranean-a SHRIMP Zircon Study. *J. Petrology*, *42*(7), 1373–1385. https://doi.org/10.1093/petrology/42.7.1373

Zeck, H. P., & Whitehouse, M. J. (2002). Repeated age resetting in zircons from Hercynian – Alpine polymetamorphic schists (Betic-Rif tectonic belt, S. Spain) - a U-Th-Pb ion microprobe study. *Chemical Geology*, *182*, 275–292. https://doi.org/https://doi.org/10.1016/S0009-2541(01)00296-0

## SUPPORTING INFORMATION

Additional Supporting Information may be found online in the supporting information tab for this article.

**Appendix S1.** Analytical details and protocols

**Appendix S2.** Zr-in-Rt thermometry

**Appendix S3.** Whole rock composition of the HP $V_1$ aluminum silicate-quartz segregations from the BM1 unit

File: Supplementary_table.xlsx

**Table S1.** List of the studied samples, with geographical location and analytical method adopted

**Table S2.** EMPA and chemical formula of White Mica

**Table S3.** EMPA and chemical formula of rutile with results of the Zr-in-Rt thermometry

**FIGURE CAPTIONS**

**Figure 1:** (a) The western Mediterranean region showing the exhumed H*P* roots of the Alpine orogen (yellow areas) and the distribution of the back-arc basins (after Jolivet et al., 2003). The Betic Rif orogen is also shown. AL: Alboran Basin, LP: Liguro-Provençal Basin, TY: Tyrrhenian Basin. (b) Schematic geological map of the Betic-Rif orogen, showing distribution of the Alboran Domain rocks in the hinterland domain showing the study area (black rectangle; modified after Michard et al., 2006, and references therein).

**Figure 2:** (a) Geological map of the Alboran Domain in the Rif belt with location of the sampling areas (modified after Kornprobst, 1975). (b) Representative pressure-temperature paths of the Alpine aged units of the Alpujarride-Sebtide complex. (c) Geological cross sections illustrating the structural architecture of the two sampled areas. (d) Cumulative stereoplot (lower hemisphere equal-area projection) showing the attitude of the $D_2$ S-L fabric in BM1. The arrow indicates the shear direction (hanging-wall movement) in non-coaxial strain domains.

**Figure 3:** (a) The $D_2$ finite strain of the BM1 at the core of the Beni Mzala antiform. Dominant coaxial stretching is documented by symmetric boudinage of the early segregated $V_1$ aluminosilicate (Ky)-quartz $V_1$ veins (exposure parallel to the X-Z section of the $D_2$ finite strain ellipsoid; core of the Beni Mzala antiform). (b) Top-to-the-NNW $D_2$ shear bands (sample B3). Kinematic indicators are provided by asymmetric boudinage and S-C fabric (exposure parallel to the X-Z section of the $D_2$ finite strain ellipsoid; core of the Beni Mzala antiform). (c) NNW-SSE trending $L_2$ stretching lineations (Chl-Qz-Wm2), nearly orthogonal to $D_2$ Chl veins (exposure parallel to the X-Y section of the $D_2$ finite strain ellipsoid; core of the Beni Mzala antiform). (d) Detail of a boundinated aluminosilicate-Quartz $V_1$ segregation (Souk el Had; sample 32).

**Figure 4:** Thin section scans of the counter face of the samples (34, 32 and B3) used for *in situ* dating. The H*P* Qz-Ky-Wm1 assemblage occurs as crenulated microlithons (relic $S_1$ foliation; dashed blue) preserved within the $S_2$ foliation (dashed green).

**Figure 5:** Mineral growth stages as referred to the tectono-metamorphic evolution of the BM1 unit as reconstructed from the textural analysis of $V_1$ aluminum (Ky)-quartz segregations.

**Figure 6:** Microtextures. (a) The $M_1$ mineral assemblage made by Qz-Ky-Wm1 in $V_1$ aluminosilicate-quartz segregations (crossed polarized light). Note the folding of the $M_1$ assemblages, preserved as microlithons within the $S_2$ spaced foliation (Sample 32). (b), (c) Enlargements of the areas indicated in (a) and (b), showing equilibrium textures between Ky and Wm1. Ky does not show any preferred orientation (crossed polarized light). (d) Deformed Ky crystals, showing evidence of bending, undulose extinction and pulled apart fractures filled by late Wm3 (crossed polarized light; Sample 34). (e) Inclusion assemblage in Ky made of Rt and Fe-Ox (Hem) (natural light; Sample B3). (f) The $M_2$ greenschist facies overprint attested by Chl-Wm2 assemblage overgrowing the Ky-Wm1 assemblage (natural light). (g), (h) Back-scattered electron (BSE) image showing the different white mica generations. (i) BSE image showing post-tectonic andalusite porphyroblast overgrowing the $S_2$ foliation in metamorphic selvage surrounding the $V_1$ aluminosilicate-quartz segregations (Sample 32).

**Figure 7:** Quartz microfabric. (a) Core-and-mantle structure defined by large relic quartz with elongated subgrains (deformation bands, DB) surrounded by fine-grained recrystallized grains (red arrows), likely formed by subgrain rotation recrystallisation (SGR). Trails of fluid inclusions (FI) can be also observed (sample 32). (b) Grain boundary migration recrystallisation (GBM) in strained quartz. Relic quartz shows undulose extinction and elongated subgrain formation (deformation bands, DB). (c), (d) Inequigranular interlobate quartz grain aggregates produced by GBM recrystallisation (sample 34). Bimodal grain size Relic quartz grains shows sweeping undulose extinction and subgrain formation (SG). Polygonisation of the recrystallized grains suggests post-deformation annealing.

**Figure 8:** (a), (b) Representative BSE images and qualitative element distribution maps for the Ky-Wm1 assemblage in sample 32 and 34, respectively (blue-green-yellow-red from low to high content). The points of EMPA are also indicated. The yellow triangles indicate the Ca-rich Wm3 (margarite/paragonite solid solutions; see Figure 8c) generations. Note the Mg-rich Wm1 core compositions. (c) White mica compositions plotted in ternary compositional diagrams. The

progressive transition from Ms-Cel solid solution to Marg-Pg solid solution is documented in the transition from Wm1 to Wm3. (d) White Mica composition. Left: $Fe^{2+}$ + Mg *vs* Si plot. Right: $Al_{TOT}$ *vs* Si plot.

**Figure 9:** *P-T* pseudosection calculated using the Perple_X software (Connolly, 2005) in the chemical system KFMASHTO ($K_2O$-FeO-MgO-$Al_2O_3$-$SiO_2$-$TiO_2$-$O_2$) for a representative $V_1$ bulk composition (wt.%): $K_2O$ = 0.48, FeO = 0.10, MgO = 0.05, $Al_2O_3$ = 12.60, $SiO_2$ = 86.24, $TiO_2$ = 0.51, $O_2$ = 0.01 for saturated $H_2O$. The dashed grey lines represent the isopleth of Si (apfu) for Wm, the blue line the Zr-in-Rt thermometry results (median value ± 1σ sd), respectively. The black arrow indicates the inferred exhumation *P-T* path followed by the BM1 unit.

**Figure 10:** (a), (c), (f), (j) Rock stubs used for *in situ* laser-probe $^{40}Ar/^{39}Ar$ geochronology of sample 34 (two stubs), 32 and B3 (from top to bottom) with the location of the areas investigated for $^{40}Ar/^{39}Ar$ laser ablation dating (yellow dotted areas). (b), (d), (g), (h), (k) Photographs of the polished section with indicated the areas for *in situ* laser analyses with distribution of $^{40}Ar/^{39}Ar$ ages. (e), (i), (m) $^{40}Ar/^{39}Ar$ age spectra as obtained from step-heating experiments on white mica grains separated from the metamorphic selvages and host rock foliation (box heights are 2σ).

**Figure 11:** (a) Cumulative probability plot of $^{40}Ar/^{39}Ar$ ages as derived from *in situ* analysis of white micas. (b) Ca/K *vs* age (error given as 2σ) correlation diagram. The light shaded area represents the Ca/K range of the analysed white micas (EMPA).

**Figure 12:** A schematic illustration of the Alpine geodynamic evolution of the Western Mediterranean region in the Eocene-Miocene time lapse (modified and re-adapted after Faccenna et al., 2004, Lacombe & Jolivet, 2005; Michard et al., 2002; Rosenbaum et al., 2002, Rossetti et al., 2013) with insets to illustrate the tectono-metamorphic evolution of the Alboran Domain. (a) The Eocene–Oligocene orogenic construction along the Apennine-Maghrebian subduction front. This stage corresponds to formation of a subduction channel where the Alboran Domain rocks are firstly subducted at depth and then exhumed to shallow crustal conditions. (b) The early Miocene collapse of the orogenic chain driven by the slab retreat. This stage corresponds to the outward migration of the compressional fronts, concomitantly with crustal thinning, high-temperature metamorphism and magmatism in the back-arc domains. Formation of the Alboran Basin in the back-arc region was accompanied by the final exhumation of the orogenic roots (Alboran Domain) in the brittle crust. Not to scale; location of structures is only indicative.

**TABLE CAPTIONS**

**Table 1:** Representative EMPA and chemical formulas of the different white mica generations

**Table 2:** *In situ* $^{40}Ar/^{39}Ar$ data

**Table 3:** $^{40}Ar/^{39}Ar$ step-heating analytical results

**Table 1 - Representative EMPA and chemical formulas of the different white mica generations**

| Group | Wm1 | | Wm2 | | Wm3 | |
|---|---|---|---|---|---|---|
| Composition | Average (*n* = 34) | Range | Average (*n* = 122) | Range | Average (*n* = 21) | Range |
| $SiO_2$ (wt.%) | 47.18 | 46.53-48.44 | 46.41 | 45.27-47.93 | 34.18 | 31.14-40.71 |
| $TiO_2$ | 0.10 | 0.01-0.35 | 0.10 | 0-0.35 | 0.03 | 0.01-0.09 |
| $Al_2O_3$ | 33.90 | 32.83-36.37 | 34.69 | 33.23-36.34 | 47.58 | 42.52-54.18 |
| FeOt | 2.20 | 0.63-3.02 | 2.47 | 1.63-3.14 | 0.50 | 0.36-0.76 |
| MnO | 0.04 | 0.02-0.07 | 0.03 | 0.01-0.07 | 0.03 | 0.02-0.05 |
| MgO | 0.95 | 0.58-1.26 | 0.77 | 0.28-1.22 | 0.27 | 0.15-0.39 |
| CaO | 0.05 | 0.02-0.12 | 0.10 | 0-0.8 | 8.66 | 4.65-10.18 |
| $Na_2O$ | 0.87 | 0.32-1.4 | 1.06 | 0.61-1.43 | 2.01 | 0.72-3.6 |
| $K_2O$ | 9.58 | 9.02-10.23 | 9.67 | 8.34-10.63 | 0.67 | 0.2-1.89 |
| BaO | 0.15 | 0.05-0.39 | 0.16 | 0-0.41 | bdl | bdl |
| Cl | bdl | bdl | bdl | bdl | bdl | bdl |
| Total | 94.90 | 93.2-96.83 | 95.31 | 93.15-96.65 | 93.89 | 91.57-95.73 |
| *Formula (11 Oxygens)* | | | | | | |
| Si (apfu) | 3.139 | 3.107-3.176 | 3.084 | 3.02-3.135 | 2.259 | 2.036-2.677 |
| Ti | 0.004 | 0-0.017 | 0.005 | 0-0.018 | 0.001 | 0-0.004 |
| $Al^{TOT}$ | 2.659 | 2.593-2.784 | 2.717 | 2.628-2.846 | 3.705 | 3.291-3.949 |
| $Al^{[IV]}$ | 0.861 | 0.824-0.893 | 0.916 | 0.865-0.98 | 1.741 | 1.323-1.964 |
| $Al^{[VI]}$ | 1.798 | 1.724-1.927 | 1.801 | 1.714-1.893 | 1.965 | 1.945-1.985 |
| $Fe^{2+}$ | 0.039 | 0-0.101 | 0.045 | 0-0.131 | - | - |
| $Fe^{3+}$ | 0.083 | 0-0.15 | 0.093 | 0.021-0.167 | 0.027 | 0.02-0.042 |
| Mn | 0.001 | 0-0.004 | 0.001 | 0-0.004 | 0.000 | 0-0.003 |
| Mg | 0.094 | 0.056-0.125 | 0.076 | 0.028-0.121 | 0.026 | 0.013-0.039 |
| Ca | 0.001 | 0-0.008 | 0.004 | 0-0.057 | 0.614 | 0.327-0.723 |
| Ba | 0.002 | 0-0.01 | 0.002 | 0-0.011 | - | - |
| Na | 0.112 | 0.041-0.18 | 0.136 | 0.078-0.182 | 0.257 | 0.087-0.461 |
| K | 0.814 | 0.763-0.86 | 0.820 | 0.704-0.898 | 0.057 | 0.017-0.159 |
| ^(a)^Ca/K [SEE ± 0.280] | 0.002 | 0-0.011 | 0.005 | 0-0.073 | 18.536 | 2.436-41.743 |
| ^(b)^$X_{Prl}$ | 0.07 | 0.02-0.13 | 0.04 | 0-0.16 | - | - |
| ^(b)^$X_{Tri}$ | 0.02 | 0.02-0.02 | 0.02 | 0.02-0.02 | - | - |
| ^(b)^$X_{Pg}$ | 0.12 | 0.05-0.18 | 0.14 | 0.09-0.19 | - | - |
| ^(b)^$X_{Cel}$ | 0.14 | 0.11-0.19 | 0.09 | 0.02-0.14 | - | - |
| ^(b)^$X_{Ms}$ | 0.65 | 0.59-0.71 | 0.71 | 0.57-0.83 | - | - |

* FeOt total iron reported as FeO; apfu: atoms per formula unit; bdl: below detection limit.
(a) Ca/K stand for Ca/K atomic ratio; Standard error of estimates (SEE) calculated using the method by Holmes and Buhr (2007).

(b) White mica molar fractions: $X_{Prl}$: pyrophyllite, $X_{Tri}$: trioctahedral substitution, $X_{Pg}$: paragonite, $X_{Cel}$: celadonite; $X_{Ms}$: muscovite. Trioctahedral substitution is fixed by stochiometry at $X_{Tri}$=0.02.

**Table 2.** ***In situ*** **$^{40}Ar/^{39}Ar$ data**

| n° | Location | $^{40}Ar/^{39}Ar$ | $^{38}Ar/^{39}Ar$ | $^{37}Ar/^{39}Ar$ | $^{36}Ar/^{39}Ar$ | $\%^{40}Ar^*$ | Age (Ma) |
|---|---|---|---|---|---|---|---|
| *Sample B3* | | | | | | | |
| 1 | Main foliation | 6.5091 | 0.0004 | 0.0000 | 0.0011 | 95.23 | 22.49 ± 1.02 |
| 2 | Main foliation | 7.0416 | 0.0000 | 0.0000 | 0.0027 | 89.78 | 24.31 ± 1.90 |
| 3 | Main foliation | 7.0090 | 0.0417 | 0.2339 | 0.0168 | 58.23 | 24.20 ± 4.21 |
| 4 | Main foliation | 6.4303 | 0.0000 | 0.1263 | 0.0017 | 92.60 | 22.22 ± 0.89 |
| 5 | Main foliation | 6.4095 | 0.0000 | 0.2337 | 0.0013 | 94.16 | 22.14 ± 0.62 |
| 6 | Main foliation | 6.5247 | 0.0000 | 0.1051 | 0.0008 | 96.39 | 22.54 ± 0.81 |
| 7 | Main foliation | 6.4075 | 0.0017 | 0.0687 | 0.0005 | 97.59 | 22.14 ± 0.49 |
| 8 | Main foliation | 6.4896 | 0.0046 | 0.0361 | 0.0000 | 99.75 | 22.42 ± 0.87 |
| 9 | Main foliation | 6.6241 | 0.0000 | 0.0260 | 0.0009 | 96.12 | 22.88 ± 0.71 |
| 10 | Main foliation | 6.4481 | 0.0018 | 0.0000 | 0.0088 | 71.03 | 22.28 ± 0.71 |
| *Sample 32* | | | | | | | |
| 1 | Ky-Qz boudin | 6.5965 | 0.0072 | 0.4049 | 0.0046 | 82.52 | 22.79 ± 1.94 |
| 2 | Ky-Qz boudin | 6.4851 | 0.0000 | 0.0414 | 0.0019 | 91.79 | 22.40 ± 0.55 |
| 3 | Ky-Qz boudin | 7.2981 | 0.0000 | 0.2923 | 0.0084 | 74.28 | 25.19 ± 2.19 |
| 4 | Ky-Qz boudin | 7.0349 | 0.0000 | 0.1868 | 0.0133 | 63.89 | 24.29 ± 3.38 |
| 5 | Ky-Qz boudin | 6.3544 | 0.0000 | 0.0000 | 0.0047 | 81.90 | 21.95 ± 0.79 |
| 6 | Ky-Qz boudin | 7.1176 | 0.0079 | 0.3171 | 0.0173 | 57.86 | 24.57 ± 1.43 |
| 7 | Ky-Qz boudin | 6.5473 | 0.0102 | 0.1289 | 0.0060 | 78.48 | 22.62 ± 0.77 |
| 8 | Ky-Qz boudin | 7.0754 | 0.0007 | 0.0758 | 0.0068 | 77.66 | 24.43 ± 0.57 |
| 9 | Ky-Qz boudin | 6.3790 | 0.0000 | 0.0180 | 0.0039 | 84.58 | 22.04 ± 0.39 |
| 10 | Ky-Qz boudin | 7.2100 | 0.0100 | 0.3985 | 0.0170 | 58.65 | 24.89 ± 1.14 |
| 11 | Ky-Qz boudin | 6.7296 | 0.0000 | 0.0413 | 0.0189 | 54.41 | 23.24 ± 0.65 |
| 12 | Ky-Qz boudin | 6.1573 | 0.0060 | 0.0198 | 0.0107 | 65.83 | 21.28 ± 0.66 |
| 13 | Ky-Qz boudin | 6.7407 | 0.0000 | 0.0806 | 0.0068 | 76.73 | 23.28 ± 0.61 |
| *Sample 34* | | | | | | | |
| 1 | Ky-Qz boudin | 6.8171 | 0.0197 | 0.7764 | 0.0049 | 82.22 | 23.54 ± 0.60 |
| 2 | Ky-Qz boudin | 8.1259 | 0.0181 | 0.0146 | 0.0074 | 78.53 | 28.03 ± 0.36 |
| 3 | Ky-Qz boudin | 7.5443 | 0.0168 | 0.0469 | 0.0193 | 56.62 | 26.04 ± 1.03 |
| 4 | Ky-Qz boudin | 7.7298 | 0.0000 | 0.1991 | 0.0259 | 49.98 | 26.67 ± 1.48 |
| 5 | Ky-Qz boudin | 7.5550 | 0.0000 | 0.2968 | 0.0044 | 84.95 | 26.07 ± 1.61 |
| 6 | Ky-Qz boudin | 6.4777 | 0.0329 | 1.5099 | 0.0040 | 84.22 | 22.38 ± 1.26 |
| 7 | Ky-Qz boudin | 8.2985 | 0.0042 | 0.1499 | 0.0037 | 88.05 | 28.62 ± 2.01 |
| 8 | Ky-Qz boudin | 6.7004 | 0.0000 | 0.2154 | 0.0048 | 82.43 | 23.14 ± 0.55 |
| 9 | Main foliation | 7.0598 | 0.0171 | 0.1681 | 0.0035 | 86.88 | 24.38 ± 1.87 |
| 10 | Main foliation | 6.8197 | 0.0000 | 0.3367 | 0.0044 | 83.85 | 23.55 ± 1.02 |
| 11 | Main foliation | 6.4914 | 0.0059 | 0.1132 | 0.0016 | 92.92 | 22.43 ± 0.81 |
| 12 | Main foliation | 7.1296 | 0.0000 | 0.2781 | 0.0021 | 91.91 | 24.62 ± 1.79 |

Errors quoted in the table are 2σ

**Table 3. $^{40}Ar/^{39}Ar$ step-heating analytical results**

| Step | $^{40}Ar/^{39}Ar$ | $^{38}Ar/^{39}Ar$ | $^{37}Ar/^{39}Ar$ | $^{36}Ar/^{39}Ar$ | $\%^{40}Ar^*$ | $\%^{39}Ar$ | Age (Ma) |
|---|---|---|---|---|---|---|---|
| *Sample B3, white mica (J=0.00193165)* | | | | | | | |
| 1 | 3.9680 | 0.0258 | 0.0020 | 5.00E-02 | 27.61 | 1.00 | 19.79 ± 3.14 |
| 2 | 8.3867 | 0.0079 | 0.0000 | 3.95E-03 | 84.37 | 1.87 | 22.26 ± 1.75 |
| 3 | 16.4279 | 0.0010 | 0.0000 | 1.96E-03 | 91.29 | 3.77 | 21.65 ± 0.83 |
| 4 | 24.9710 | 0.0267 | 0.0000 | 1.05E-03 | 95.30 | 5.46 | 22.73 ± 0.63 |
| 5 | 14.0589 | 0.0145 | 0.0890 | 5.05E-04 | 97.60 | 3.09 | 22.60 ± 1.11 |
| 6 | 20.6396 | 0.0148 | 0.0510 | 6.34E-04 | 96.93 | 4.70 | 21.82 ± 0.72 |
| 7 | 80.9694 | 0.0000 | 0.0871 | 3.85E-04 | 98.06 | 18.37 | 21.89 ± 0.18 |
| 8 | 67.6426 | 0.0186 | 0.0000 | 2.64E-04 | 98.61 | 15.45 | 21.74 ± 0.22 |
| 9 | 45.6427 | 0.0000 | 0.0603 | 2.63E-04 | 98.61 | 10.43 | 21.74 ± 0.32 |
| 10 | 51.1594 | 0.0000 | 0.0635 | 5.23E-04 | 97.38 | 11.90 | 21.36 ± 0.27 |
| 11 | 35.5178 | 0.0000 | 0.0000 | 6.93E-04 | 96.60 | 8.27 | 21.33 ± 0.40 |
| 12 | 34.8728 | 0.0000 | 0.0000 | 4.65E-04 | 97.69 | 7.94 | 21.81 ± 0.41 |
| 13 | 11.5496 | 0.0000 | 0.0000 | 0.00E+00 | 99.85 | 2.53 | 22.70 ± 0.83 |
| 14 | 6.6009 | 0.0000 | 0.0000 | 3.56E-04 | 98.23 | 1.46 | 22.39 ± 2.36 |
| 15 | 5.7089 | 0.0000 | 0.0000 | 2.09E-03 | 90.85 | 1.30 | 21.82 ± 2.48 |
| 16 | 11.3236 | 0.0416 | 0.0000 | 8.86E-03 | 71.20 | 2.47 | 22.80 ± 1.53 |
| | | | | | | | Total age: **21.83 ± 0.15** |
| *Sample 32, white mica (J=0.0019278)* | | | | | | | |
| 1 | 5.0298 | 0.0000 | 0.0000 | 2.51E-01 | 9.64 | 0.65 | 27.64 ± 4.58 |
| 2 | 8.6222 | 0.0135 | 0.0000 | 1.82E-02 | 60.00 | 1.09 | 28.22 ± 2.76 |
| 3 | 144.8685 | 0.0000 | 0.0000 | 2.17E-03 | 90.71 | 23.36 | 22.25 ± 0.13 |
| 4 | 116.9052 | 0.0000 | 0.0000 | 1.63E-04 | 99.09 | 19.15 | 21.90 ± 0.16 |
| 5 | 51.2601 | 0.0000 | 0.0000 | 1.33E-04 | 99.22 | 8.38 | 21.95 ± 0.36 |
| 6 | 62.7866 | 0.0000 | 0.0000 | 1.34E-04 | 99.23 | 10.23 | 22.02 ± 0.30 |
| 7 | 17.3539 | 0.0000 | 0.0702 | 2.09E-04 | 98.90 | 2.78 | 22.42 ± 1.10 |
| 8 | 13.8826 | 0.0000 | 0.0000 | 0.00E+00 | 99.85 | 2.23 | 22.36 ± 1.00 |
| 9 | 52.0643 | 0.0000 | 0.0000 | 3.84E-04 | 98.12 | 8.33 | 22.43 ± 0.38 |
| 10 | 38.4059 | 0.0027 | 0.0000 | 2.30E-04 | 98.78 | 6.26 | 21.99 ± 0.50 |
| 11 | 23.0942 | 0.0000 | 0.0000 | 0.00E+00 | 99.85 | 3.77 | 21.97 ± 0.60 |
| 12 | 15.5774 | 0.0000 | 0.0000 | 0.00E+00 | 99.85 | 2.58 | 21.66 ± 0.84 |
| 13 | 67.6887 | 0.0319 | 0.0000 | 1.06E-04 | 99.35 | 11.20 | 21.68 ± 0.27 |
| | | | | | | | Total age: **22.15 ± 0.12** |
| *Sample 34, white mica (J=0.0019306)* | | | | | | | |
| 1 | 10.3847 | 0.0000 | 0.0000 | 3.77E-02 | 39.04 | 0.64 | 25.03 ± 1.53 |
| 2 | 14.1504 | 0.0000 | 0.0109 | 5.01E-03 | 82.22 | 0.91 | 24.12 ± 0.97 |
| 3 | 14.1238 | 0.0000 | 0.0000 | 2.76E-03 | 88.77 | 0.96 | 22.87 ± 0.80 |
| 4 | 20.2821 | 0.0000 | 0.1750 | 2.53E-03 | 89.22 | 1.43 | 22.02 ± 0.68 |
| 5 | 107.5929 | 0.0000 | 0.0000 | 1.02E-03 | 95.34 | 7.54 | 22.19 ± 0.40 |
| 6 | 159.8785 | 0.0000 | 0.0989 | 3.66E-04 | 98.16 | 11.28 | 22.03 ± 0.28 |
| 7 | 103.1061 | 0.0200 | 0.1254 | 1.53E-04 | 99.14 | 7.28 | 22.02 ± 0.42 |
| 8 | 120.4835 | 0.0476 | 0.0000 | 1.71E-04 | 99.05 | 8.55 | 21.91 ± 0.36 |
| 9 | 48.3586 | 0.0000 | 0.0157 | 0.00E+00 | 99.85 | 3.43 | 21.89 ± 0.52 |
| 10 | 250.1017 | 0.0086 | 0.0738 | 1.44E-04 | 99.17 | 17.82 | 21.82 ± 0.19 |
| 11 | 109.3824 | 0.0000 | 0.0000 | 6.92E-05 | 99.52 | 7.77 | 21.90 ± 0.39 |
| 12 | 99.1353 | 0.0000 | 0.1441 | 2.73E-04 | 98.56 | 7.10 | 21.72 ± 0.42 |
| 13 | 94.0583 | 0.0000 | 0.2444 | 0.00E+00 | 99.85 | 6.71 | 21.79 ± 0.28 |
| 14 | 91.5516 | 0.0000 | 0.0394 | 3.20E-05 | 99.70 | 6.50 | 21.88 ± 0.47 |
| 15 | 54.8000 | 0.0000 | 0.1550 | 0.00E+00 | 99.85 | 3.90 | 21.84 ± 0.46 |
| 16 | 26.4097 | 0.0000 | 0.0000 | 0.00E+00 | 99.85 | 1.90 | 21.65 ± 0.93 |
| 17 | 42.5481 | 0.0000 | 0.0000 | 0.00E+00 | 99.85 | 3.05 | 21.66 ± 0.58 |
| 18 | 45.1867 | 0.0000 | 0.0000 | 0.00E+00 | 99.85 | 3.22 | 21.81 ± 0.55 |
| | | | | | | | Total age: **21.94 ± 0.12** |

Errors quoted in the table are 2σ

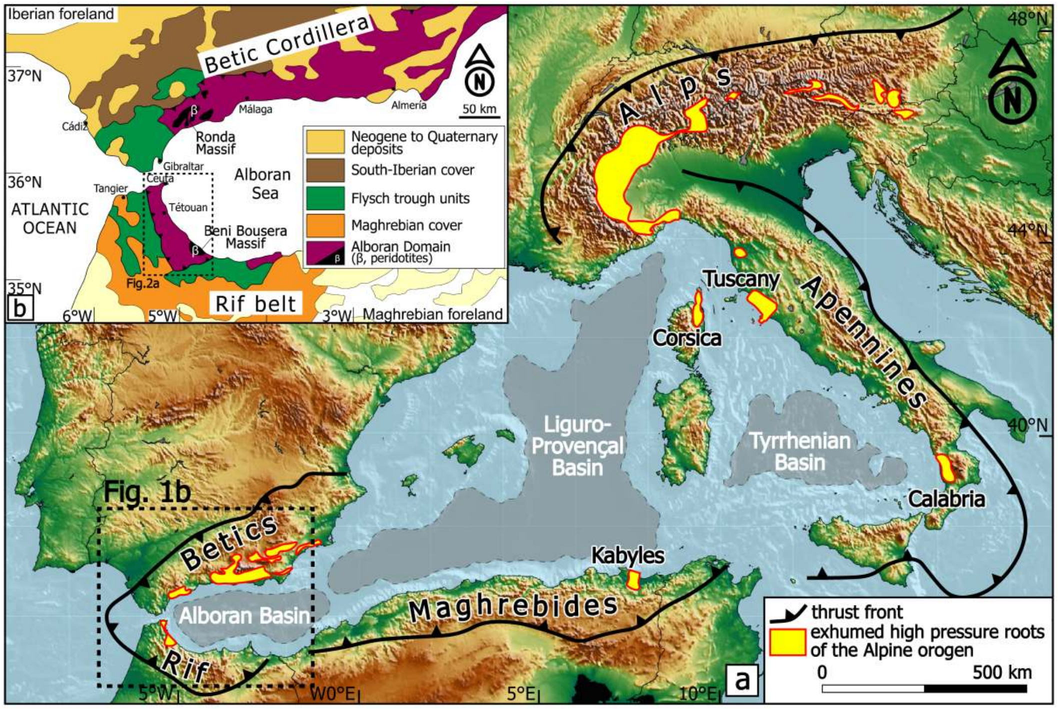


jmg_12587_f1.png

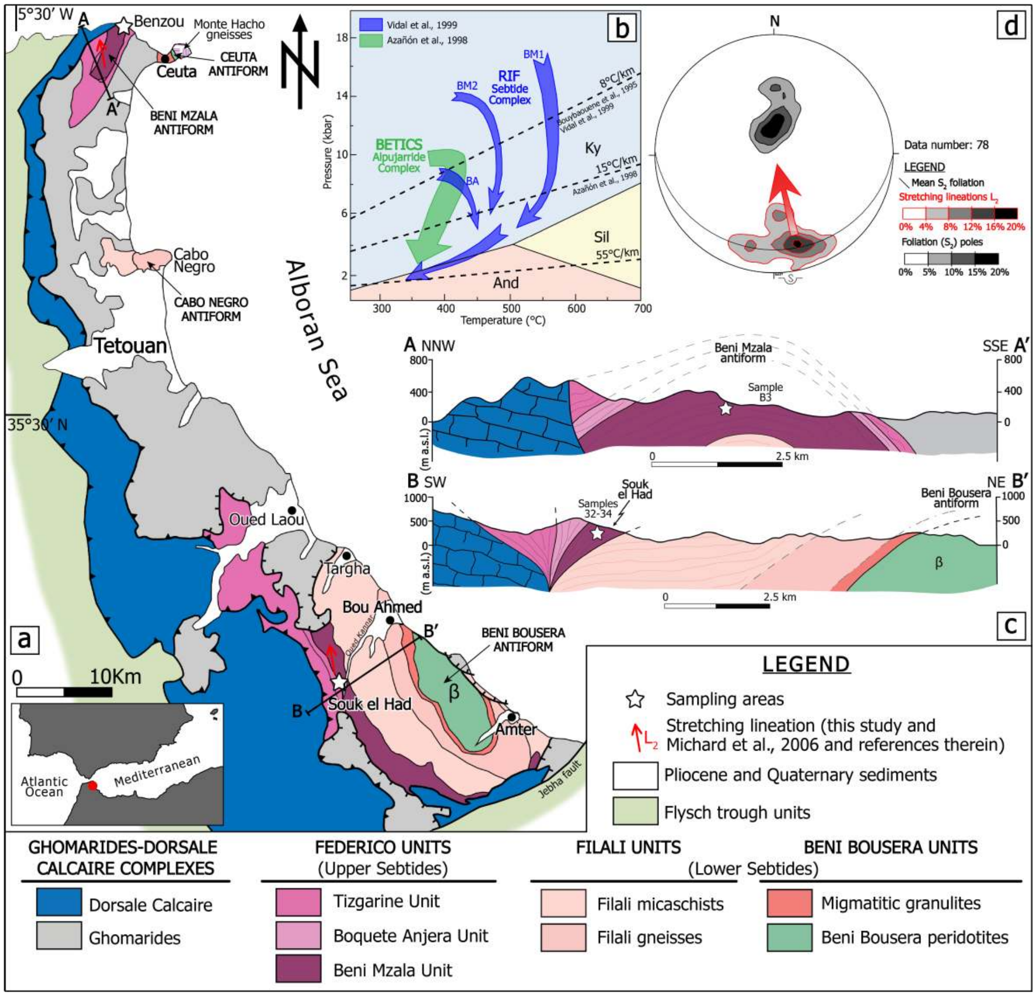


jmg_12587_f2.png

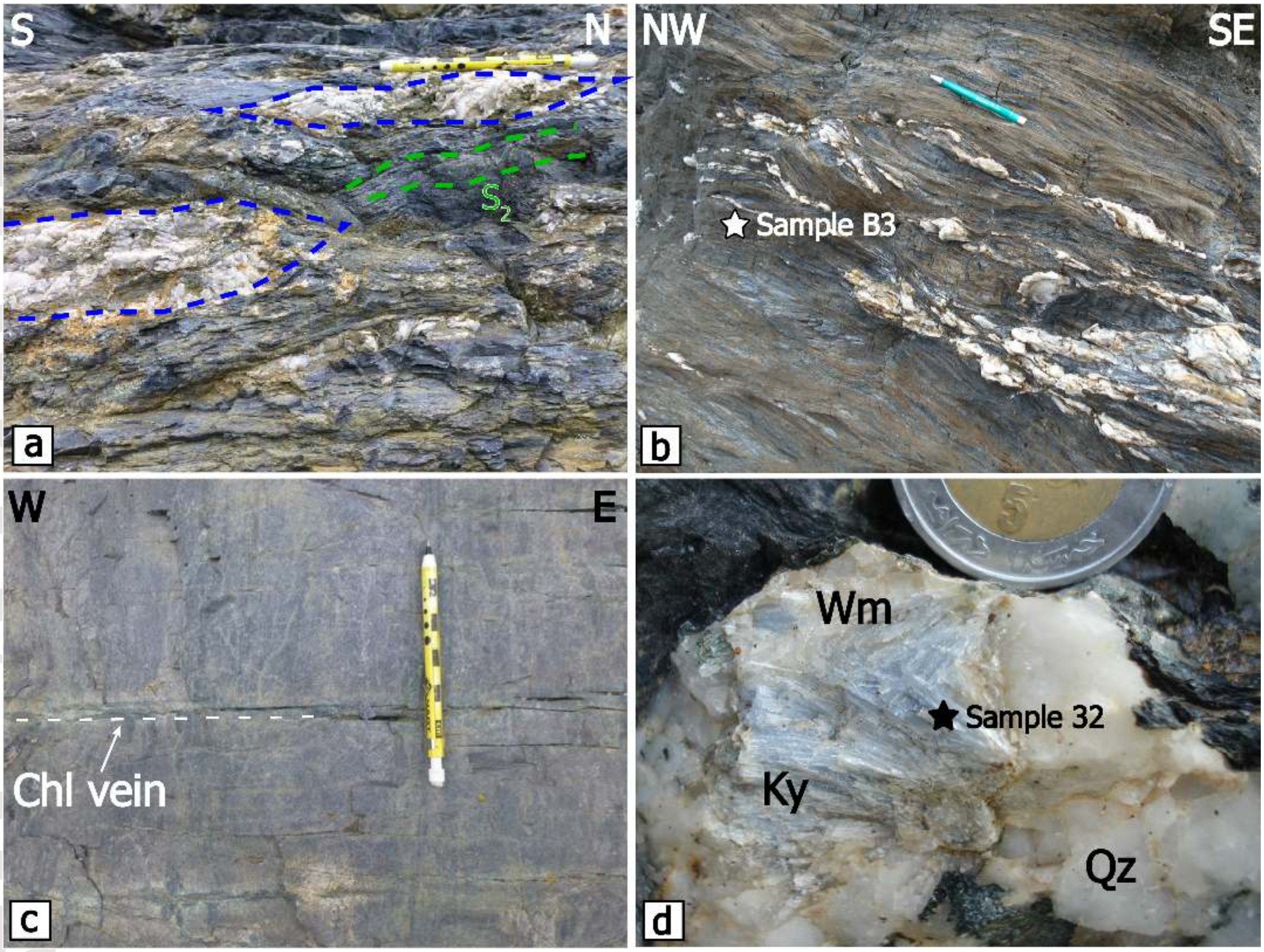


jmg_12587_f3.png

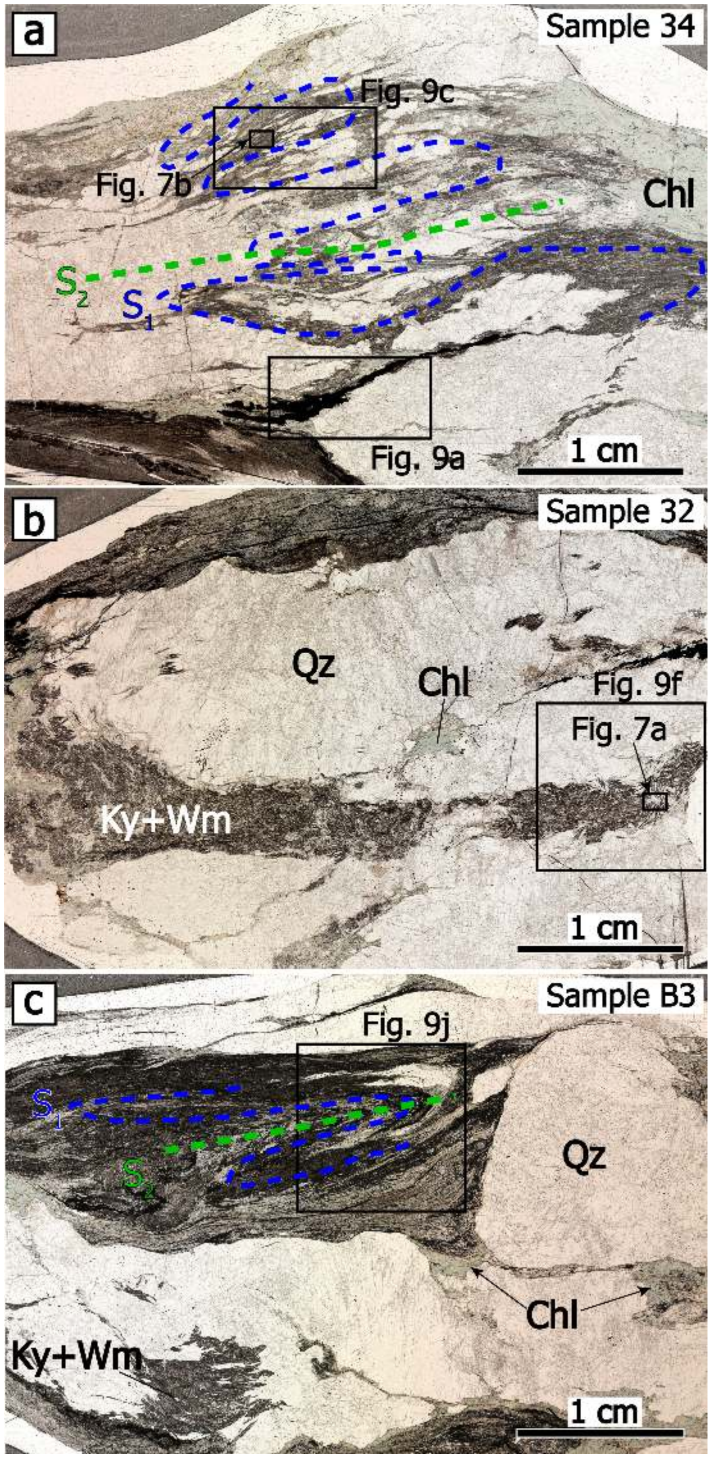


jmg_12587_f4.png

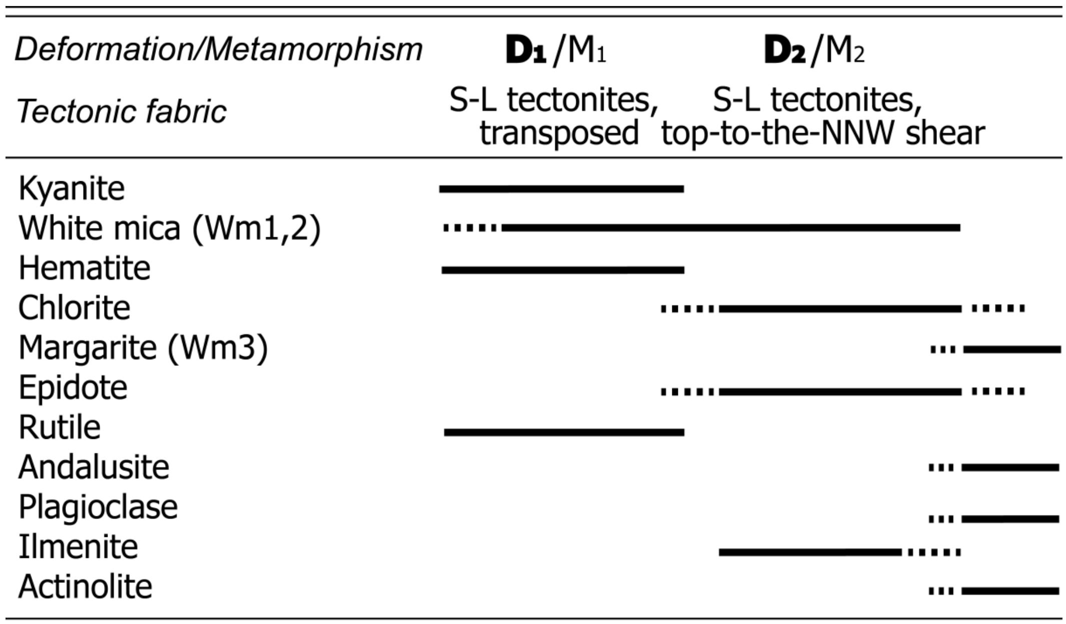


jmg_12587_f5.png

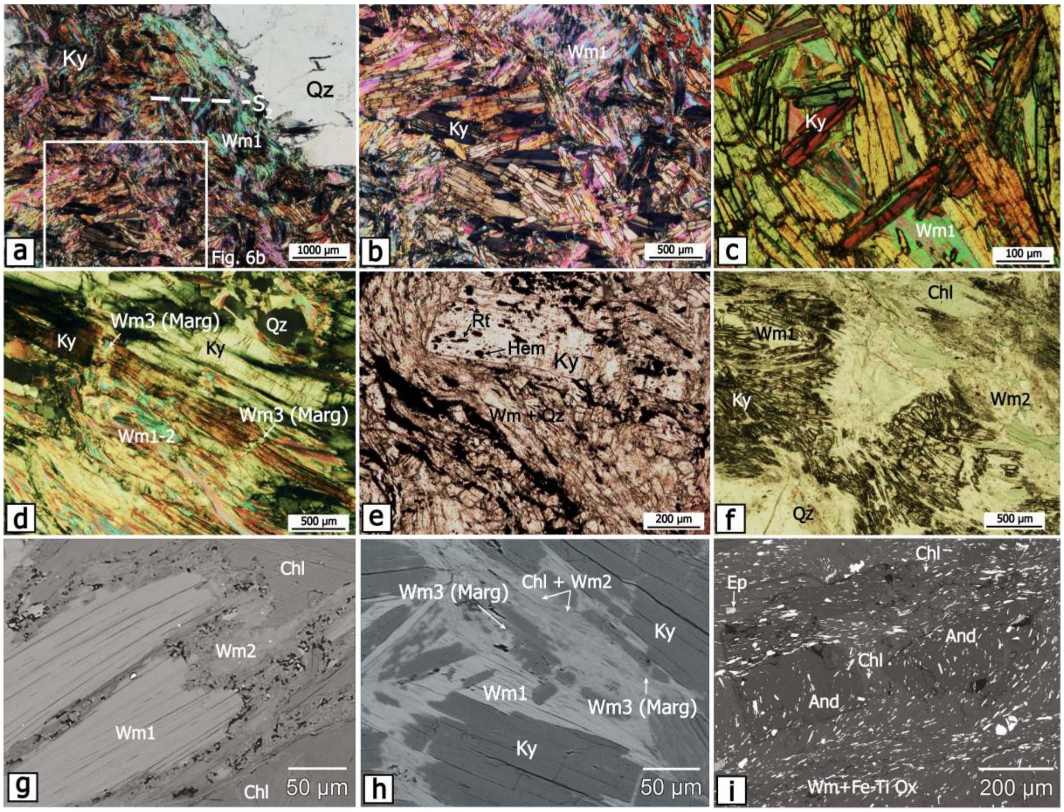


jmg_12587_f6.png

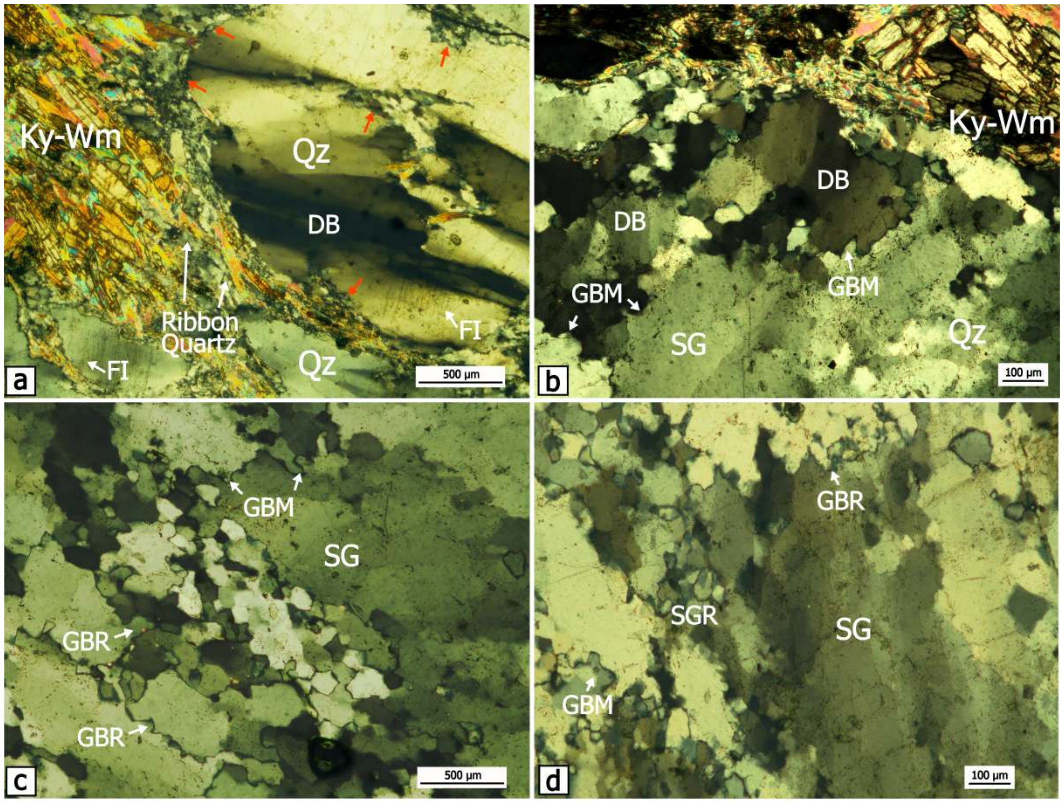


jmg_12587_f7.png

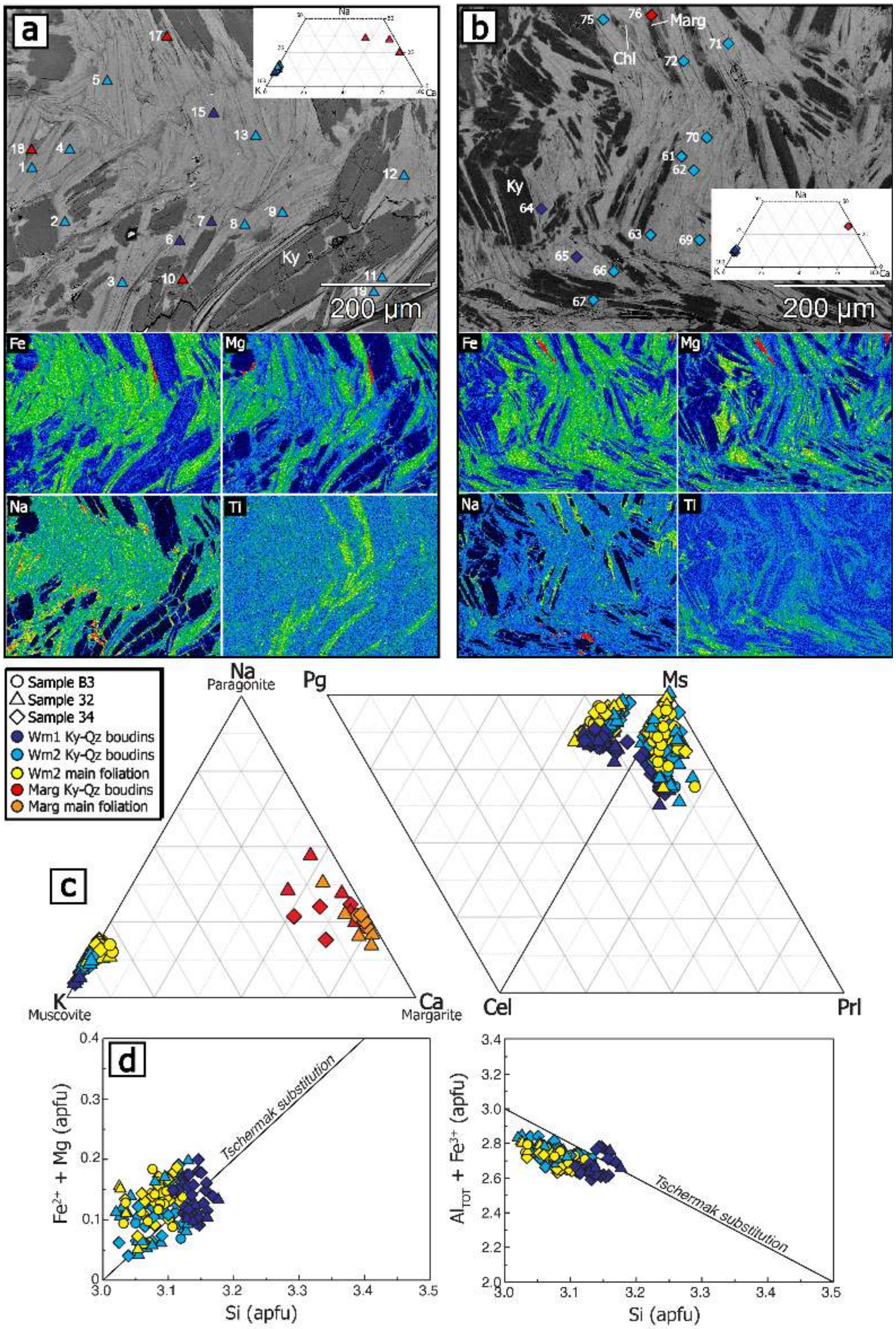


jmg_12587_f8.png

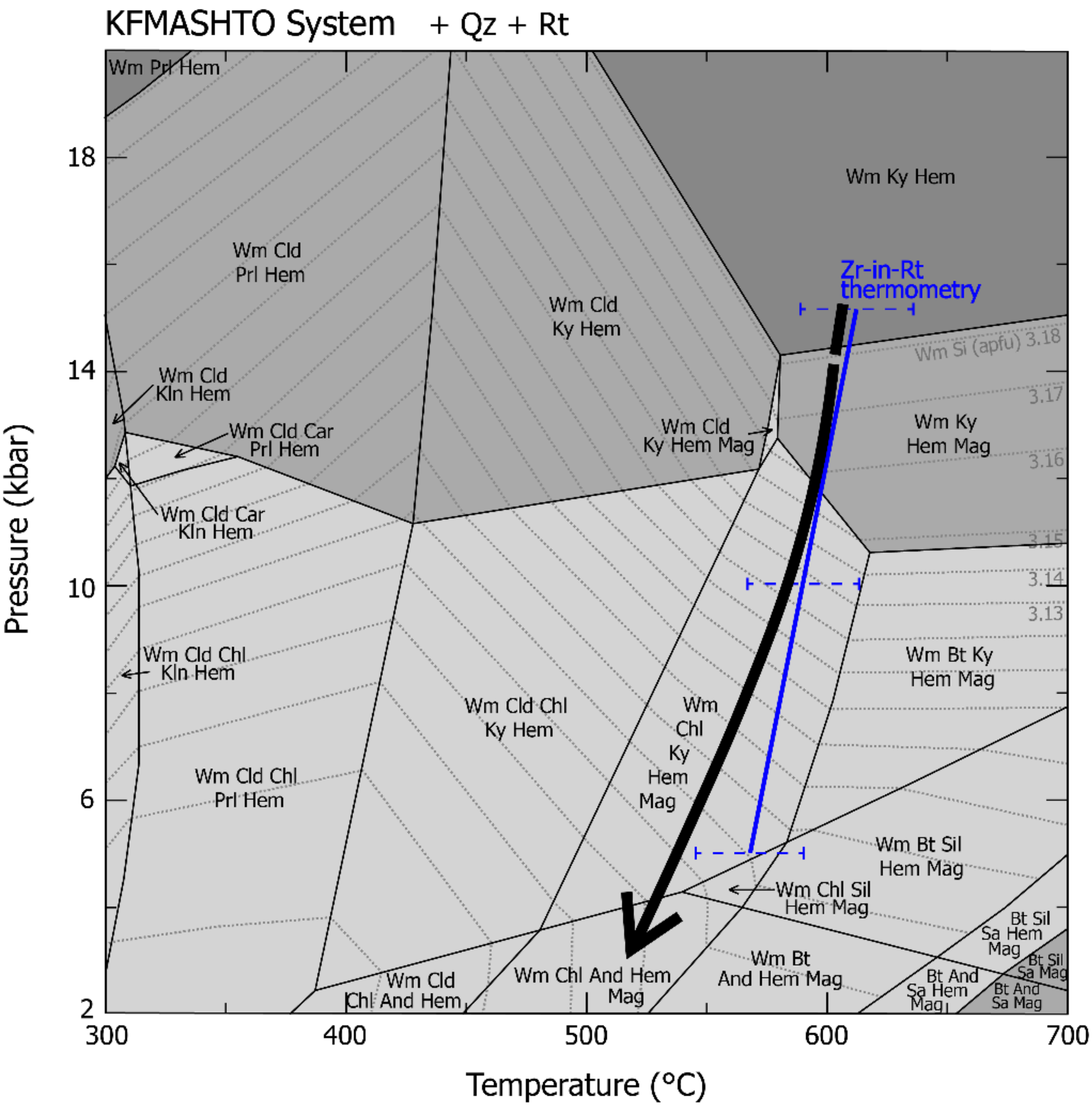


jmg_12587_f9.png

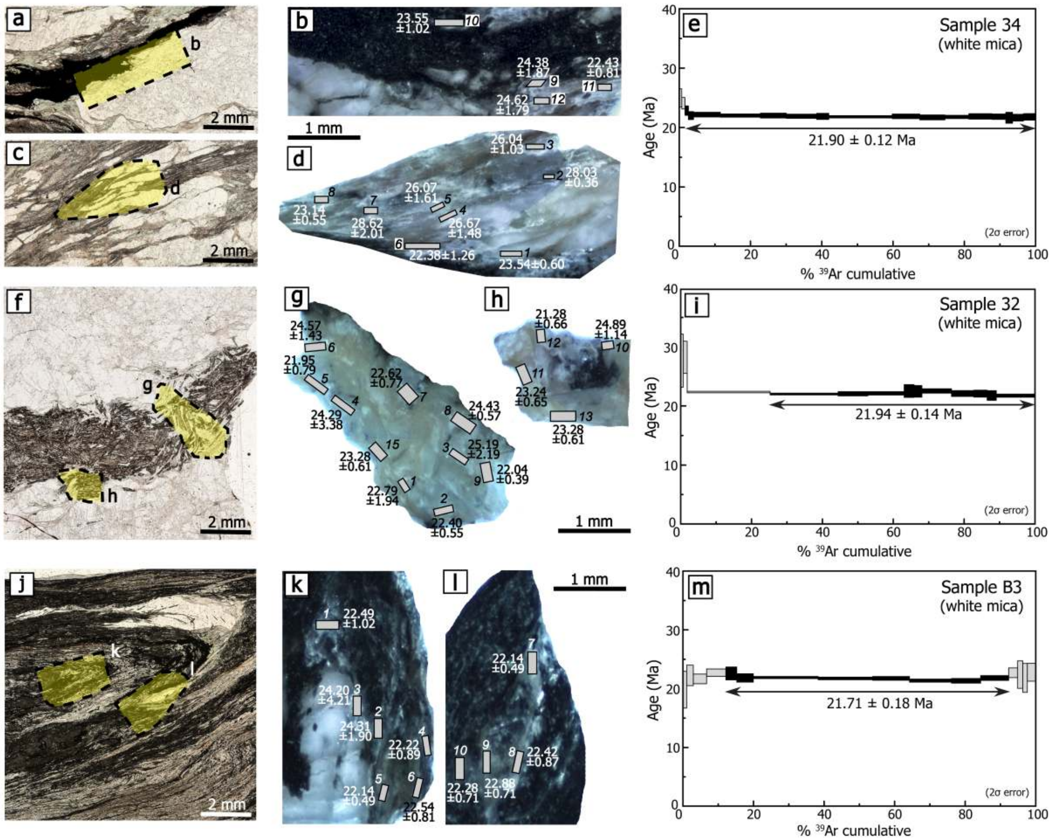


jmg_12587_f10.png

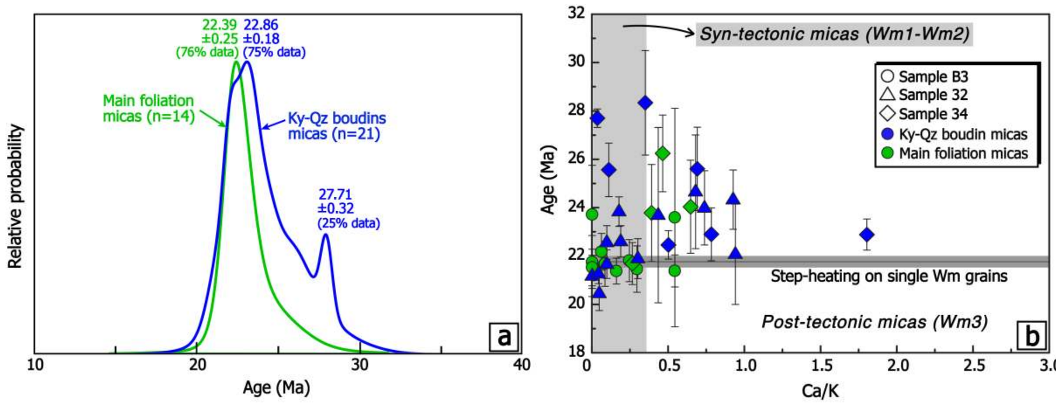


jmg_12587_f11.png

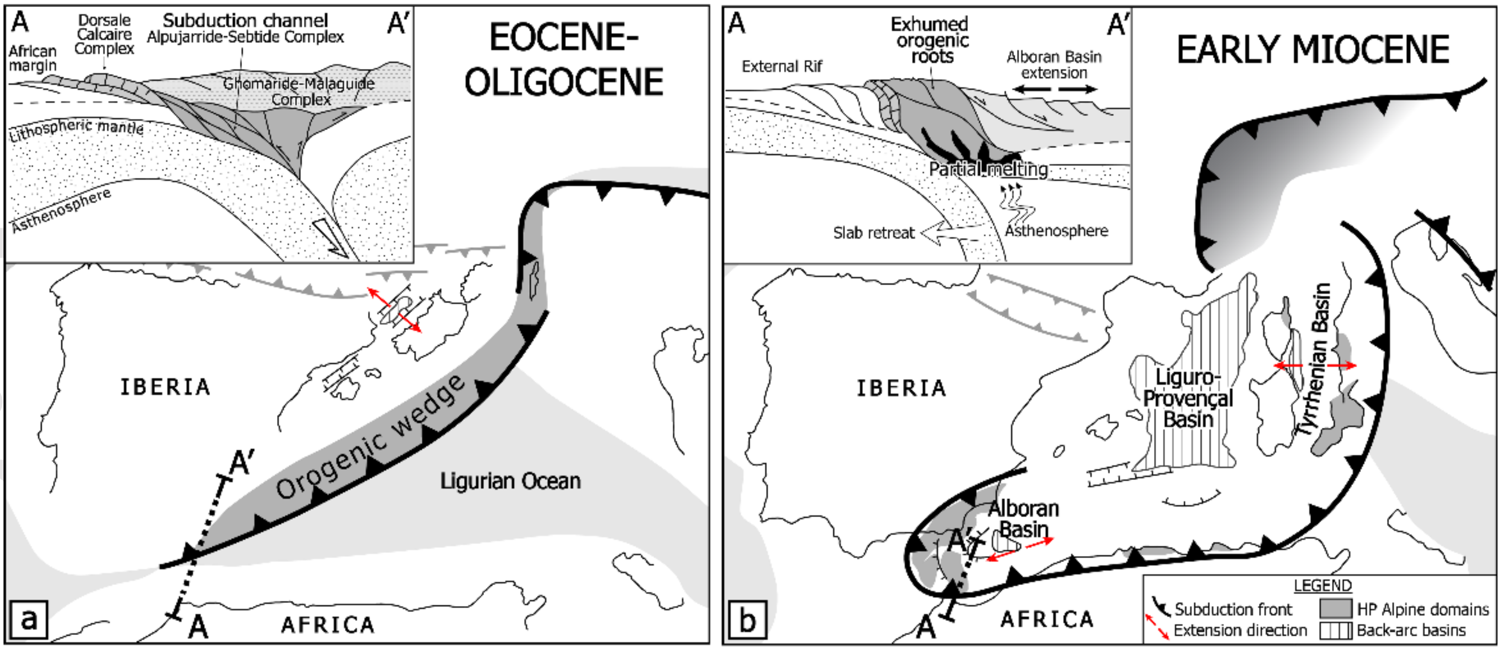


jmg_12587_f12.png